Bulge n and B/T in High Mass Galaxies

Tim Weinzirl[1], Shardha Jogee[1], Sadegh Khochfar[2], Andreas Burkert[3], John Kormendy(?)[1]

ABSTRACT

The properties of galaxy components provide key constraints for models of galaxy evolution. With an iterative $2D$ decomposition technique based on GALFIT, we perform bulge-disk and bulge-disk-bar decomposition on H-band images of ~ 150 moderately inclined ($i \leq 70°$) spiral galaxies with $M_B \leq -19.3$ from the OSU Bright Spiral Galaxy Survey. The sample has primarily spirals with Hubble type S0/a to Sc and stellar mass $M_* \geq 1.0 \times 10^{10} M_\odot$. Our results are: (1) We find that 53.4% of our sample requires bulge-disk-bar decomposition. The resulting H-band bar fraction is 58.2%. For galaxies with $M_* \geq 1.0 \times 10^{10} M_\odot$, we find that 20.4% of stellar mass is in bulges (with 15.7% in $n > 2$ bulges and 4.7% in $n \leq 2$ bulges), 69.6% in disks, and 10.0% in stellar bars. (2) Only a small fraction (5.5%) of bulges have classical Sérsic indexes ($n \geq 4$): such bulges lie primarily in S0/a to Sab, and have large $B/T > 0.2$. A large fraction (34.4%) of bulges have $2 < n < 4$: they exist in barred and unbarred S0/a to Sd, and their B/T spans a wide range (0.03 to 0.5) with a mean of 0.23. Finally, 60.2% of bulges have $n \leq 2$: they exist in barred and unbarred galaxies across all Hubble types; their B/T spans a wide range (0.01 to 0.4) with a mean of 0.10. (3) Furthermore, bulges with $B/T \leq 0.2$ are pervasive and exist across the whole spectrum of S0/a to Scd. For $M_* \geq 1.0 \times 10^{10} M_\odot$, $\sim 66\%$ of spiral galaxies have $B/T \leq 0.2$. In comparing with ΛCDM-based models, it is found that the distribution in B/T of spirals with bulges built by major mergers sersiously underpredicts the observed abundance of low B/T systems. Most galaxies in the models experience only minor mergers, and on the whole ΛCDM-based models agree well with the data provided almost all $B/T < 0.2$ systems are built from minor mergers. (4) We revisit bulge formation in hierarchical models of galaxy evolution. We suggest that the three types of bulges ($n \geq 4$, $2 < n < 4$, $n \leq 2$) have different formation origins. The hybrid $2 < n < 4$ bulges likely form in major mergers that

---

[1]Department of Astronomy, University of Texas at Austin, Austin, TX

[2]Sub-Department of Astrophysics, University of Oxford, Denys Wilkinson Bldg., Keble Road, OX1 3RH, Oxford, UK

[3]Universitäts-Sternwarte München, Scheinerstr. 1, 81679 München, Germany

have residual gas left over after violent relaxation, or in minor mergers. Low $n \leq 2$ bulges likely form from gas inflows driven by bars and minor mergers at late-epochs, and possibly in major mergers of low mass ratios (e.g., 1:3 or lower).

1. Introduction

The formation of galaxies is a classic problem in astrophysics. Contemporary galaxy formation models combine the well-established Λ Cold Dark Matter (ΛCDM) cosmology, which describes behavior of dark matter on very large scales, with baryonic physics to model galaxy formation. In the early Universe, pockets of dark matter decoupled from the Hubble flow, collapsed into virialized halos, and then clustered hierarchically into larger structures. Meanwhile, gas aggregated in the interiors of the halos to form rotating disks, which are the building blocks of galaxies (Steinmetz & Navarro, 2002; Cole et al. 2000). Such disks are typically destroyed during major mergers of galaxies with mass ratio $M_1/M_2 > 1/4$ (e.g., Steinmetz & Navarro, 2002; Burkert & Naab, 2004; Mihos & Hernquist 1996). When the mass ratio is close to unity and star formation (SF) efficiency is high, the remnant is a spheroid with properties close to that of a classical bulge, namely a steep de Vaucouleurs $r^{1/4}$ surface brightness profile and a high ratio of random-to-ordered motion (V/σ). The question of what happens in major mergers of lower mass ratio, higher gas fractions, and lower SF efficiency has not yet been explored in detail, and in fact, has only been addressed by a few simulations. We shall return to this point in § 5. Within this hierarchical framework, the disk of spiral galaxies forms when gas of higher specific angular momentum subsequently accretes around the bulge (Steinmetz & Navarro, 2002; Burkert & Naab, 2004).

Troubling inconsistencies appear to exist between real galaxies and ΛCDM-based simulations of galaxy formation. One issue is the angular momentum problem; simulated galaxy disks have smaller scalelengths and, therefore, less specific angular momentum than their counterparts in nature (Burkert & D'Onghia, 2004; D'Onghia et al. 2006). A second problem is the severe under prediction in the frequency of galaxies with no bulges (so-called bulgeless galaxies) or generally with low bulge-to-total mass ratio (B/T). Within the ΛCDM paradigm, every galaxy that had a past major merger at a time when its mass was a fairly large fraction of its present-day mass, is expected to have a significant bulge with large B/T and high Sérsic index, while galaxies of low B/T or without bulges are expected to be rare. Yet there is rising evidence that reality is quite different. Kautsch et al. (2006), as well as Barazza, Jogee & Marinova (2007; 2008) find from the analysis of several thousand late-type SDSS galaxies that 15-20% of such disk galaxies out to $z \sim 0.03$ are bulgeless. Locally, late-type Sd galaxies often harbor no bulge (Böker et al. 2002). The trouble posed by the absence of classical bulges becomes more puzzling when pseudobulges are acknowledged. Pseudobulges are an additional complication because they are built by secular processes rather than mergers (Kormendy & Fisher 2005; Kormendy 2007). Of the 19 local galaxies ($D < 8Mpc$) with $V_c > 150$ kms^{-1}, 11 (58%) have pseudobulges instead of merger-built classical bulges (Kormendy 2008). Completely resolving the issue of low B/T systems will require folding in pseudobulges and secular evolution.

The emerging statistics on the fraction of bulgeless ($B/T \sim 0$) galaxies in low mass spirals from the above studies (Kautsch et al. 2006; Barazza, Jogee & Marinova 2008; Kormendy 2008), provide important first constraints. However, many questions still remain unanswered. What is the distribution of B/T ratios along the Hubble sequence, in both high mass and low mass galaxies? How does this distribution compare to predictions from hierarchical models of galaxy evolution? Is there a discrepancy between models and observations only for bulgeless ($B/T \sim 0$) systems, or for a spectrum of low B/T values? What is the nature of galaxies with low B/T, in terms of their mass distribution, SF history, and merger history? These investigations can help us understand the formation pathways of low B/T galaxies, and provide clues on what aspects of the baryonic physics in ΛCDM-based simulations need to be modified in order to solve the discrepancies. In this paper we attempt to address these questions.

The structural properties of galaxy components, such as bulges, disks, and bars can be derived through the decomposition of the 2D light distribution, taking into account the PSF. Many early studies have performed only two component bulge-disk decomposition (e.g., Allen et al. 2006; Byun & Freeman 1995; de Jong 1996; Simard 1998; Wadadekar et al. 1999), ignoring the contribution of the bar, even in strongly barred galaxies. However, recent work has shown that it is important to include the bar in $2D$ decomposition of barred galaxies, else the B/T ratio can be artificially inflated, and bulge properties skewed (e.g., Laurikainen et al. 2005, 2007; Balcells and Graham, in preparation). Furthermore, since most ($\geq 60\%$) bright spiral galaxies are barred in the NIR (Eskridge et al. 2000; Laurikainen et al. 2004; Marinova & Jogee 2007, hereafter MJ07; Menendez-Delmestre et al. 2007), the inclusion of the bar is quite important. This has led to several recent studies, where $2D$ bulge-disk-bar decomposition are being performed (e.g., Laurikainen et al. 2007; Reese et al. 2007; Gadotti & Kauffman 2007).

Another advantage of bulge-disk-bar decomposition over bulge-disk decomposition is that the former allows us to constrain the properties of the bar itself. Bars provide the most important internal mechanism for redistributing angular momentum in baryonic and dark matter components (e.g., Weinberg 1985; Debattista & Sellwood 1998, 2000; Athanassoula 2002; Berentzen, Shlosman, & Jogee 2006). They efficiently drive gas inflows into the central kpc, feed central starbursts (Elmegreen 1994; Knapen et al. 1995; Hunt & Malakan 1999; Jogee et al. 1999; Jogee, Scoville, & Kenney 2005; Jogee 2006) and lead to the formation of disky, high V/σ stellar components in the inner kpc, or 'pseudobulges' (Kormendy 1993; Jogee 1999; review by Kormendy & Kennicutt 2004; Jogee, Scoville, & Kenney 2005; Athanassoula 2005). Furthermore, the prominence of strong bars out to $z \sim 1$ over the last 8 Gyr (Jogee et al. 2004; Sheth et al. 2008) suggest that bars have been present over cosmological times and can shape the dynamical and secular evolution of disks. Thus, quantifying bar properties, such as the fractional light and mass ratio (Bar/T), can yield insight into these processes.

In this paper, we constrain the properties of bulges and bars along the Hubble sequence, and compare our results to ΛCDM-based simulations of galaxy evolution. Our sample consists of $\sim$ 150 moderately inclined spirals from the Ohio State University Bright Spiral Galaxy Survey (OSUBSGS; Eskridge et al. 2002), which is widely used as the local reference sample for bright spirals by numerous studies (e.g., Eskridge et al. 2000; Block et al. 2002; Buta et al. 2005; MJ07 ; Laurikainen et al. 2004, 2007). The sample is dominated by galaxies with $M_B \sim$ -19.3 to -23.0, stellar mass $M_* \geq 1.0 \times 10^{10} M_\odot$, and Hubble types in the range S0/a to Sc (§ 2). In § 3, we perform $2D$ bulge-disk and bulge-disk-bar decompositions of H-band images using GALFIT (Peng et al. 2002), and derive fractional light ratios (B/T, Bar/T, Disk/T), as well as Sérsic indexes and half light radii or scale lengths. Tests to verify the robustness of our decompositions are presented in § 4. In § 5, we present our results. Specifically, the total stellar mass present in bulges, disks, and bars is calculated § 5.2. In § 5.3, the distribution of bulge Sérsic index n and B/T as a function of galaxy Hubble type and stellar mass is presented, and the surprising prevalence of bulges with low Sérsic index n and low B/T established. A comparison with other works is presented in § 5.4. In § 5.5, we compare our cumulative fraction of galaxies as a function of B/T to that predicted by ΛCDM-based hierarchical simulations of galaxy evolution, and show that the models agree with the distribution of B/T for high mass ($M_* \geq 1.0 \times 10^{10} M_\odot$) galaxies. In § 5.6, we revisit bulge formation in hierarchical models of galaxy formation and suggest that the three types of bulges ($n \geq 4$, $2 < n < 4$, $n \leq 2$) have different formation origins. We examine how Bar/T changes as a function of host galaxy properties in § 5.7. In § 5.8 we examine how bar fraction changes with B/T and bulge index. § 6 summarizes our results.

2. Sample Properties

2.1. OSUBSGS

Our dataset is derived from the 182 H-band images from the public data release of the Ohio State University Bright Spiral Galaxy Survey (OSUBSGS; Eskridge et al. 2002). These galaxies are a subset of the RC3 catalog that have $m_B \leq 12$, Hubble types $0 \leq T \leq 9$, $D_{25} \leq 6'.5$, and $-80^\circ < \delta < +50^\circ$. Imaging of OSUBSGS galaxies spans optical and near infrared (NIR) wavelengths with $BVRJHK$ images available for most galaxies. We choose to use the NIR images rather than optical ones for several reasons. Firstly, NIR images are better tracers of the stellar mass than optical images, and the mass-to-light ratio is less affected by age gradients or dust gradient. Secondly, obscuration by dust and SF are minimized in the NIR, compared to the optical. As the K-band images are of poor quality, we settle on using the H-band images.

The OSUBSGS is widely used as the local reference sample for bright spirals by numerous studies (e.g., Eskridge et al. 2000; Block et al. 2002; Buta et al. 2005; MJ07 ; Laurikainen et al. 2004, 2007). Thus, there are numerous complementary results that we can use or compare to. In particular, MJ07 have identified bars in this sample using quantitative criteria based on ellipse fitting, and characterized their ellipticities.

OSUBSGS is a magnitude-limited survey ($m_B \leq 12$) with objects whose distances range up to ~ 60 Mpc. Faint galaxies are inevitably missed at larger distances, resulting in the absolute magnitude distribution in Figure 1. We compare the B-band LF of this sample with a Schechter LF (SLF) with $\Phi^* = 5.488 \times 10^{-3}$ Mpc^{-3}, $\alpha = -1.07$, and $M_B^* = -20.5$ (Efstathiou, Ellis & Peterson, 1988) in Figure 3. The volume used to determine the number density in each magnitude bin is

$$V_{max} = \frac{4\pi}{3} d_{max}^3(M) f_{sky}, \tag{1}$$

where

$$d_{max}(M) = 10^{1+0.2(m_c - M)} \tag{2}$$

and f_{sky} is the fractional sky solid angle observed (59%). d_{max} is the maximum distance out to which a galaxy of absolute magnitude M can be observed given the cutoff magnitude m_c (12 for OSUBSGS in the B band). If the SLF is representative of the true LF, then Figure 3 suggests that the OSUBSGS sample starts to be seriously incomplete at $M_B > -19.3$, while at the brighter end (-19.3 to -23) the shape of its LF matches fairly well the SLF. We thus conclude that the sample is reasonably complete for bright ($M_B < -19.3$ or $L_B > 0.33$ L^*) galaxies.

We further exclude highly inclined ($i > 70°$) galaxies for which structural decomposition does not yield accurate results. Thus, our final sample consists of $\sim$ 150 moderately inclined $i \leq 70°$) spirals with $M_B \sim$ -19.3 to -23.0 (Figure 1). The Hubble types are mainly in the range S0/a to Sc (Figure 2), and we estimate that the galaxies have stellar masses $M_\star \geq 1.0 \times 10^{10} M_\odot$ (see § 2.2; Figure 4). Table 1 summarizes the morphologies, luminosities, and stellar masses of the sample. Note that there are few galaxies of late Hubble types (Scd or later) and we do not draw any conclusions on such systems from our study. In paper II, we will tackle galaxies of lower mass and later Hubble types by using UKIRT Infrared Deep Sky Survey (Warren et al. 2007) data for a sample of SDSS galaxies.

2.2. Stellar Masses

We derive global stellar masses for most of the OSUBSGS sample galaxies using the relation between stellar mass and rest-frame $B - V$ color from Bell et al. (2003). Using population synthesis models, the latter study calculates stellar M/L ratio as a function of color using functions of the form $log_{10}(M/L) = a_\lambda + b_\lambda \times Color + C$, where a_λ and b_λ are bandpass dependent constants and C is a constant that depends on the stellar initial mass function (IMF). For the V band Bell et al. (2003) find $a_\lambda = -0.628$ and $b_\lambda = 1.305$; assuming a Kroupa (1993) IMF, they find C = -0.10. This yields an expression for the stellar mass in $M_\odot$ for a given $B - V$ color:

$$M_\star = v_{lum} 10^{-0.628+1.305(B-V)-0.10}, \tag{3}$$

where

$$v_{lum} = 10^{-0.4(V-4.82)}. \tag{4}$$

Here, V_{lum} is the luminosity parametrized in terms of absolute V magnitude.

How reliable are stellar masses determined from this procedure? Clearly, the above relationship between M_* and $B - V$ cannot apply to all galaxies, and must depend on the assumed stellar IMF, and range of ages, dust, and metallicity. However, it is encouraging to note that several studies (Bell et al. 2003; Drory et al. 2004) find generally good agreement between masses based on broad-band colors and those from spectroscopic (e.g., Kauffmann et al. 2003a b) and dynamical (Drory et al. 2004) techniques. Typical errors are within a factor of 2 to 3.

We used this relation to compute stellar masses for 127 (87%) objects. The remainder did not have $B-V$ colors available in the Hyperleda database or RC3. The mass distribution is summarized in Figure 4. Individual masses are listed in Table 1.

3. Method and Analysis

The structural properties of galaxy components, such as bulges, disks, and bars can be derived through the decomposition of the 2D light distribution, taking into account the PSF. There are several softwares for $2D$ luminosity decomposition, including GIM2D (Simard et al. 2002), GALFIT (Peng et al. 2002), and BUDDA (de Souza et al. 2004). The latter two allow bulge-disk-bar decomposition to be fitted, while the former only allows bulge-disk decomposition

Most previous work has addressed $2D$ bulge-disk decomposition only. Allen et al. (2006), for example, performed bulge-disk decomposition with GIM2D on 10,095 galaxies from the Millennium Galaxy Catalog (Liske et al. 2003; Driver et al. 2005). However, recent work (e.g., Laurikainen et al. 2005; Graham & Balcells, in preparation) has shown that the B/T ratio can be artificially inflated in a barred galaxy unless the bar component is included in the $2D$ decomposition. The fact that most ($\geq 60\%$) bright spiral galaxies are barred in the NIR (Eskridge et al. 2000; Laurikainen et al. 2004; MJ07; Menendez-Delmestre et al. 2007), further warrants the inclusion of the bar. Another advantage of bulge-disk-bar decomposition is that it allows us to constrain the properties of the bar itself, and to constrain scenarios of bar-driven secular evolution (see § 1).

Motivated by these considerations, several studies have tackled the problem of $2D$ bulge-disk-bar decomposition. Laurikainen et al. (2005, 2007) have developed a $2D$ multicomponent decomposition code designed to model bulges, disks, primary and secondary bars, and lenses; they apply Sérsic functions to bulges and use either Sérsic or Ferrers functions to describe bars and lenses. Reese et al. (2007), have written a non-parametric algorithm to model bars in ~ 70 I-band images. Gadotti & Kauffman (2007) are performing $2D$ bulge-disk-bar and bulge-disk decomposition of 1000 barred and unbarred galaxies from SDSS with the BUDDA software.

In this study we perform 2D bulge-disk decomposition and three-component bulge-disk-bar decomposition of the OSUBSGS sample with GALFIT. We note that Laurikainen et al. (2007) have also performed bulge-disk-bar decomposition on the OSUBSGS sample. However, there are also important complementary differences between our study and theirs. The technique softwares, and tests on the robustness performed in our study are different (see § 3 and § 4). Furthermore, unlike Laurikainen et al. (2007), we also compare the B/T to predictions from hierarchical models of galaxy evolution (§ 5), and present the distribution of Bar/T.

3.1. Image Preparation

Running GALFIT on an image requires initial preparation. The desired fitting region and sky background must be known, and the PSF image, bad pixel mask (if needed), and pixel noise map must be generated. We addressed these issues as follows: (1) The GALFIT fitting region must be large enough to include the entirety of the galaxy, including the outer galaxy disk. Since cutting out empty regions of sky can drastically reduce GALFIT run-time, a balance was sought between including the entire galaxy and excluding as much empty sky as possible; (2) It is possible for GALFIT fit the sky background, but this is not recommended. When the sky is a free parameter, the wings of the bulge Sérsic profile can become inappropriately extended, resulting in a Sérsic index that is too high. Also, fitting the sky requires the fitting region to be as large as possible, increasing the run-time. Sky backgrounds were measured separately and designated as fixed parameters; (3) GALFIT requires a PSF image to correct for seeing effects. Statistics of many stars in each frame can be used to determine an average PSF. However, many of our images contain only a few stars. Instead, a high S/N star from each frame was used as a PSF; (4) We used ordered lists of pixel coordinates to make bad pixel masks, which are useful for blocking out bright stars and other image artifacts; (5) We had GALFIT internally calculate pixel noise maps for an image from the noise associated with each pixel. Noise values are determined from image header information concerning gain, read noise, exposure time, and the number of combined exposures.

3.2. Decomposition Steps

Figure 5 summarizes our method of decomposition, which we now detail. GALFIT requires initial guesses for each component it fits. It uses a Levenberg-Marquardt downhill-gradient algorithm to determine the minimum χ^2 based on the input guesses. GALFIT continues iterating until the χ^2 changes by less than 5e-04 for five iterations (Peng et al. 2002). We recognize that a drawback to any least-squares method is that a local minimum, rather than a global minimum, in χ^2 space may be converged upon. We explore this possibility with multiple tests described in §4. We adopted an iterative process, involving three separate invocations of GALFIT, to perform 1-component, 2-components, and 3-components decomposition:

1. Stage 1 (single Sérsic): In Stage 1, a single Sérsic component is fitted to the galaxy. This serves the purpose of measuring the total luminosity, which is conserved in later Stages, and the centroid of the galaxy, which is invariant in later fits.

2. Stage 2 (exponential plus Sérsic): In Stage 2, the image is fit with the sum of an exponential disk and a Sérsic component. During the Stage 2 fit, the disk b/a and PA are held constant at values, which we take from the published ellipse fits of MJ07, as well as ellipse fits of our own. This procedure reduces the number of free parameters in the fit by fixing the disk b/a and PA, which are easily measurable parameters. It also prevents GALFIT from confusing the disk and bar, and artificially stretching the disk along the bar PA in an attempt to mimic the bar. As initial guesses for the Sérsic component in Stage 2, the output of Stage 1 is used. The Sérsic component in Stage 2 usually represents the bulge, in which case Stage 2 corresponds to a standard bulge-disk decomposition

   However, in a few rare cases, where the galaxy only has a bar and a disk, the Sérsic component in Stage 2 represents a bar. The latter is recognizable by a low Sérsic index and large half light radius.

3. Stage 3 (exponential plus two Sérsic components): In Stage 3, a three-component model consisting of an exponential disk, a Sérsic bulge, and a Sérsic bar is fit. As suggested by Peng et al. (2002), the bar can be well described by an elongated, low-index Sérsic ($n < 1$) profile. As in Stage 2, the disk b/a and PA are held constant at values predetermined from ellipse fits. We provide initial guesses for the bar b/a and PA, based on ellipse fits of the images from MJ07 or analysis of the images in DS9. We provide GALFIT with input guesses for the bulge parameters, based on the output from Stage 2. In principle, it is also possible to generate reasonable guess parameters for the bulge and disk from a bulge-disk decomposition on a $1D$ profile taken along a select PA (Kormendy, private communication). As described in § 4.3, we also experiment with initial guesses derived in this way, and find that the final convergence solution is the same. We also note that GALFIT fixes the bulge b/a and does not allow it to vary with radius, while real bulges may have a varying b/a. We tested the impact of fixed and varying bulge b/a on the derived B/T (§ 4.1) and find that there is no significant change in B/T.

For objects with an AGN or a compact nuclear cluster, the bulge Sérsic index in the Stage 2 and Stage 3 models could grow excessively high, reaching values up to 20. We attended to this problem by fitting a PSF as a fourth component to all 49 objects whose initial fits had bulge Sérsic indexes > 5. Twenty-eight of these objects are classified as AGN, based on the catalogs of Ho et al. (1997), Veron Catalog of Quasars & AGN, 12th Edition (Véron-Cetty & Véron 2006), and NED. Six extra objects are known to not be AGN but are identified by Ho et al. (1997) as having HII nuclei. The remaining 15 objects do not have published nuclear line ratios to indicate if they host AGN. However, all appear to have bright compact nuclear sources, which could be nuclear star clusters or AGN. The fractional luminosities of the PSF components (PSF/T) are typically a few percent or less, with several being $< 1\%$; a few are between 5-7%, and these are all confirmed AGN. The PSF luminosity was added back to the bulge in calculating B/T. Since PSF/T is generally small, this step introduces only a small change in the final B/T of the relevant galaxies.

GALFIT also allows a diskiness/boxiness parameter to be added to any Sérsic and exponential profile. We did not use this parameter for any bulge or disk profiles. Bars in general have boxy isophotes, and we could have included the diskiness/boxiness parameters in the bar profiles. However, it was found that adding the parameter to the bar profile did not change the model parameters significantly, even though the appearance of the residual images improved in some cases. As accounting for bar boxiness would have only made a small-to-negligible change in the derived structural parameters, we chose to neglect bar boxiness altogether.

3.3. Choosing the Best Fit Between Stage 2 and Stage 3

All objects in our sample were subjected to Stages 1, 2, and 3. Depending on whether a galaxy with a bulge is unbarred or barred, its best fit should be taken from the Stage 2 bulge-disk decomposition or the Stage 3 bulge-disk-bar decomposition, respectively. For objects with prominent bars, it is obvious that the Stage 3 model provides the best fit. However, it is more difficult to decide between Stage 2 versus Stage 3 fits in galaxies, which host weak bars with no strong visual signature. In practice, we therefore applied the set of criteria below to each galaxy in order to select between the Stage 2 bulge-disk decomposition and Stage 3 bulge-disk-bar decomposition. Table 2 lists the model chosen for each galaxy, as well as bulge, disk, and bar structural parameters.

For completeness, we note that for the few rare galaxies (see § 3.2), which only have a bar and a disk, the choice of a final solution is between the Stage 2 bar-disk decomposition and Stage 3 bulge-disk-bar decomposition. The same criteria below can be used to identify the best model.

1. GALFIT calculates a χ^2 and χ^2_ν for each model. It was found that χ^2 almost universally declines between the Stage 2 and Stage 3 fits for a given object. This is because in the Stage 3 fit, five extra free parameters (bar luminosity, r_e, Sérsic index, b/a, and PA) are added with the Sérsic bar component, allowing GALFIT to almost always make a lower χ^2 model during Stage 3. However, this does not necessarily mean that the solution in Stage 3 is more correct physically. Thus, an increasing χ^2 was interpreted

as a sign that the Stage 3 fit should not be adopted, but an increasing χ^2 was not considered as a sufficient condition to adopt Stage 3.

2. In cases with prominent bars, a symmetric light distribution due to unsubtracted bar light was often found in the Stage 1 and Stage 2 bulge-disk residuals. This was strong evidence that the Stage 3 bulge-disk-bar fit be selected. NGC 4643 is shown in Figure 6 because it has a particularly striking bar residual; the corresponding fit parameters appear in Table 4.

3. The Stage 2 and Stage 3 models were only selected so long as the model parameters were all well behaved. In unbarred galaxies, the Stage 3 model parameters might be unphysically large or small, in which case the Stage 2 fit was favored. Conversely, in galaxies with prominent bars, the bulge component of the Stage 2 bulge-disk fit tends to grow too extended in size. Addition of a bar in the Stage 3 bulge-disk-bar fit removes this artifact, giving a more physical solution. An extreme example of this situation is the barred galaxy NGC 4548, which has a prominent bar and a faint disk. The Stage 2 fit, based on a Sérsic bulge and exponential disk, is highly inadequate to describe the bulge, disk, *and* the bar. It leads to an extremely extended bulge. The Stage 3 bulge-disk-bar fit, however, yields a believable fit with a prominent bar. The results of Stage 1, Stage 2, and Stage 3 are displayed in Figure 7 and Table 5.

4. Not all barred galaxies had unphysical Stage 2 models. Instead, the bulge could be stretched along the PA of the bar, giving the bulge a lower Sérsic index and larger effective radius. A Stage 3 model that returned the bulge to a size and shape more representative of the input image was favored over the Stage 2 fit. Figure 8 demonstrates this behavior in NGC 4902. We distinguish this effect from cases like NGC 4548 (Figure 7) where the Stage 2 fit is completely wrong.

5. In cases where there was no bar, GALFIT can sometimes be enticed into fitting a bar to any existing spiral arms, rings, or the clumpy disks of late-type spirals. Stage 3 fits in these cases could be discarded by noting the resulting discrepancies in appearance between the galaxy images and the Stage 3 model images. Examples of false bars are shown in Figure 9.

4. Extra Tests to Verify Correctness of Fits

4.1. Varying b/a as a Function of Radius

Models generated with GALFIT do not allow the b/a of the bulge, disk, or bar to vary with radius. Since real bulges may have a varying b/a, it is legitimate to investigate what is the impact of fixing the bulge b/a, on the estimated B/T. We therefore performed the following test on NGC 4548 . To mimic a model bulge of varying b/a, we fitted the bulge light of NGC 4548 with ten concentric Sérsic profiles of increasing r_e and varying b/a. The r_e of the outermost profile comes from the original bulge model (see Table 5) where b/a was kept constant with radius. The separation in r_e between adjacent profiles is 0.5 pixels (0.75”). The luminosity, Sérsic index, b/a, and PA of each profile were free parameters. The disk and bar components were fixed to the values in Table 5, as the emphasis was on the change in bulge only.

Figure 10 shows the range in b/a (0.85 to 1.0) and PA ($-90°$ to $+90°$) of the bulge profiles. The outermost PA is quite close the $-66.5°$ value from the single-component bulge model. The Sérsic indexes were generally higher toward the center and declined at larger r_e, indicating the bulge is more concentrated at the center. The B/T of the ten bulge models combined is 14.5%, in close agreement with results obtained with a single component is used for the bulge. It appears that restricting the bulge b/a to remain constant across radius does not significantly affect our derived B/T.

4.2. Fitting Artificially Simulated Images

An elementary test is to determine if GALFIT can recover the known parameters of artificially simulated noisy images. The images were simulated by taking parametric model images produced by GALFIT, and adding noise to the images with the PyFITS module for Python (Barrett & Bridgman, 1999). Noise was calculated by adding in quadrature the noise due to the source, sky, read noise, and a random number drawn from a Gaussian distribution scaled by a fraction of the sky background. The standard deviation of pixel noise in electrons was computed as

$$\sigma = \sqrt{N_{source} + N_{sky} + N_{read}^2 + N_{random} \times f \times N_{sky}}, \tag{5}$$

where the scale factor f was set to 0.5. The offset added to each pixel value was drawn from a normal distribution centered at 0 with standard deviation σ.

Our test sample consisted of six bulge-disk-bar and four bulge-disk models with two models of each group containing extra PSF components. Examples of the artificially simulated noise-added models are shown in Figure 11. These images were subjected to the 2D decomposition procedure outlined in Figure 5. GALFIT reproduced the known parameters quite closely. The mean surface brightness inside the disk scalelength spanned 4.5 magnitudes. B/T and D/T were recovered to within $\pm 5\%$ in most cases. In a few cases, the deviation was as high as $\pm 10\%$.

In addition, for the models with PSFs, very high Sérsic indexes were obtained in the Stage 2 and Stage 3 fits before extra PSF components were added to the models. The success of this test is evidence that GALFIT is able to converge to the absolute minimum in χ^2 space for our bulge-disk and bulge-disk-bar decompositions when the input is the sum of parametric functions.

4.3. Using $1D$ Decomposition To Generate Guesses for Bulge Parameters

It is important to verify that GALFIT converges to the same solution even if the initial guesses for the bulge parameters in Stage 2 and 3 are different. Bulge-disk decomposition from $1D$ profiles provides an alternative means of generating initial guesses. While $1D$ bulge-disk decompositions of radial profiles along the bar major axis can be influenced by the bar, decomposition of cuts along the bar minor axis will not be influenced as heavily. The resulting bulge and disk parameters should be adequate guesses for Stage 3 of our $2D$ decomposition method (Kormendy, private communication).

We tested the robustness of our Stage 3 fits by extracting initial guesses for the bulge and disk using $1D$ decomposition along the bar minor axis. The nonlinear least-squares algorithm designed to perform the $1D$ decomposition simultaneously fits the sky-subtracted profiles with the sum of a Sérsic bulge and an exponential disk, while ignoring the PSF. The results from the $1D$ decomposition include a bulge magnitude, r_e, Sérsic index, disk magnitude, and disk scalelength.

The robustness of several bulge-disk-bar fits were tested by using the results of the $1D$ decomposition as input to Stage 3. The $1D$ decompositions do not provide information about the axis ratio (b/a) or PA, so these parameters for the bulge were estimated by eye; for the disk, the b/a and PA were fixed to the values determined by ellipse fitting, as described in §3.2. The initial bar parameters were unchanged from the earlier Stage 3 fits. In all cases, the new models were identical to the Stage 3 models. As an example, Table 3 compares Stage 3 input derived from 1D decomposition and GALFIT for NGC 4548 and NGC 4643. In each case, both sets of input reproduced the same results.

5. Results and Discussion

5.1. Impact of Bars in $2D$ Decomposition

From the Stage 2 bulge-disk decomposition and Stage 3 bulge-disk-bar decompositions, which we performed on all objects (§ 3.2) we saw firsthand the effects of adding a bar to the fit of a barred galaxy. We summarize below some of these effects in order to underscore the importance of including a bar component in the $2D$ luminosity decomposition of barred galaxies

1. During the Stage 2 bulge-disk decomposition of a barred galaxy, the luminosity which comes from the galaxy's disk, bulge, *and bar* gets distributed only between two model components : the model bulge and disk. Since the disk b/a and PA are measured independently and held constant during the fits, the Stage 2 model tends to distort the bulge in order to fit the bar. Thus, the bulge in the Stage 2 bulge-disk decomposition of a barred galaxy can be artificially long or too bright and extended. When a model bar component is added in the Stage 3 bulge-disk-bar decomposition of a barred galaxy, it forces a reshuffling of the luminosity between the three components. Generally, the bulge declines in luminosity, whereas light can be either taken from, or added back, to the disk.

2. We find that the inclusion of a bar component in the Stage 3 bulge-disk-bar decomposition of a barred galaxy reduces the bulge fractional luminosity B/T, compared to the Stage 2 bulge-disk decomposition. For our 77 barred galaxies, the reductions correspond to factors of less than 2, 2 to 4, and above 4, in 34%, 28%, and 38% of barred galaxies, respectively. The larger changes in B/T occur in very strongly barred galaxies, where a prominent bar cause the Stage 2 bulge-disk decomposition to overestimate the bulge. For instance, B/T declines in both of NGC 4643 (Figure 6 and Table 4) and NGC 4548 (Figure 7 and Table 5). In the latter case, B/T is reduced by a factor of 5 between Stage 2 and Stage 3. These examples underscore the importance of including bars in $2D$ luminosity decomposition of very strongly barred galaxies.

3. The scalelength of the disk is generally unchanged by including the bar. NGC 4548 (Figure 7 and Table 5) is a good example. Sometimes, however, the disk from the Stage 2 bulge-disk decomposition of a barred galaxy is erroneous due to a poor fit. The disk parameters from the Stage 3 bulge-disk-bar decomposition are quite different in such cases. NGC 4643 (Figure 6 and Table 4) illustrates this behavior.

We find that out of the 146 moderately inclined spirals ($i \leq 70°$) in our sample, 53.4% are better fit with a Stage 3 bulge-disk-bar decomposition than a Stage 2 bulge-disk decomposition. The resulting H-band bar fraction, defined as the fraction of disk galaxies that are barred, is 58.2%. This fraction is in excellent agreement with the H-band bar fraction of 60% reported by MJ07 based on ellipse fits of the same sample, with a more conservative inclination cut ($i \leq 60°$). Furthermore, as a check to our fits, we compare the bar and unbarred classification for individual galaxies from our fits to those from MJ07, which were based on ellipse fits. Of the 74 galaxies that we classify as barred and which are mutually fitted by MJ07, 55 (74.3%) are also classified as barred by MJ07. The remaining 19 (25.7%) galaxies are mainly weakly barred (with Bar/T below 0.08). Their RC3 optical types are weakly barred AB (10), barred B (7), and unbarred A (2).

5.2. Mass in Bulges, Disks, and Bars

The fractional H-band luminosities in the bulge, disk, and bar (B/T, D/T, Bar/T) of each galaxy can be considered as a fractional mass if we assume that the same mass-to-light (M/L) ratio in the H band can be used for all three components. This is not an unreasonable assumption as the H-band M/L ratio is not very sensitive to dust or age gradients in intermediate age stellar populations. Population synthesis models allow M/L of galaxies to be determined based in their observed spectral energy distributions. Relying on different input stellar models and spectra creates a dispersion of predictions and implies uncertainties in the results. Charlot, Worthey, & Bressan (1996) find for idealized galaxies with a single generation of stars that such uncertainties in mass determination are roughly $\pm 35\%$ for a fixed metallicity and IMF.

For galaxies with high star formation rates and populations of massive, young stars, assuming a constant M/L ratio underestimates stellar mass. An unintentional consequence is that the B/T fractional mass in galaxies with central star formation could be understated To test this possibility, the H-band images were inspected for signs of central star formation. Only about 20% of galaxies show signs of clumpiness and starbursts, so the majority of objects appear to not have bursts of central star formation. The distribution of B/T discussed in §5.3 and §5.5 are unlikely to be affected much by assuming a constant M/L ratio in the H band.

Using the total galaxy stellar mass from § 2.2, the fractional masses can be converted into absolute masses. (We do not convert the H-band luminosity directly into a mass as the H-band images do not have photometric calibration). The results are shown in Table 6. For galaxies with $M_* \geq 1.0 \times 10^{10} M_\odot$, we find that 20.4% of stellar mass is in bulges (with 15.7% in $n > 2$ bulges and 4.7% in $n \leq 2$ bulges), 69.6% in disks, and 10.0% in stellar bars. Figure 12 shows the stellar mass for bulges, disks, and bars, respectively, along the Hubble sequence.

5.3. Distribution of Bulge Index and B/T

Figure 13 shows the individual and mean B/T and bulge Sérsic index, plotted, as a function of Hubble type and galaxy stellar mass. Barred and unbarred galaxies are shown separately. Figure 14 shows the relationship between bulge index and B/T.

We first consider the B/T values in Figure 13. The mean B/T in barred galaxies is lower than in unbarred galaxies, but there is a large overlap in the individual values. The offset in the mean B/T of barred and unbarred galaxies reported here, agrees with the result of Laurikainen et al. (2007; see § 5.4) on the same sample. We also note that B/T does not correlate with Bar/T (Fig. 15) : aside from the 6 galaxies with large Bar/T (> 0.3), most galaxies have moderate Bar/T and a wide range of B/T is seen at each Bar/T. This is reassuring and suggests that the bar fit is not arbitrarily biasing the B/T values. The distribution of Bar/T is further discussed in §5.7.

How does the B/T vary as a function of Hubble type and galaxy stellar mass? Bulges with very high B/T (> 0.4) exist primarily in galaxies with high mass ($M_* > 6 \times 10^{10} M_\odot$) and early types (S0/a to Sab). Bulges with very low B/T (< 0.1) lie primarily in lower mass galaxies with later morphologies (Sb to Sc). However, it is striking that bulges with $B/T \leq 0.2$ are pervasive and exist across the whole spectrum of S0/a to Scd. We shall return to this point in §5.5.

Some of the low $B/T \leq 0.2$ values for six barred S0/a and Sa on Figure 13 may at first look suspicious. However, visual inspection of their images shown in (Figure 16) shows that the bulges do not seem very conspicuous compared to the disk, and suggests that the measured low B/T values are in fact reasonable. It is likely that these galaxies were assigned early Hubble types due to their smooth extended disks, rather than a high bulge-to-disk ratio. Similarly, some of the high $B/T \sim 0.4$ value in three of the Scs may at first look odd. However, again, visual inspection of their image (Figure 16) suggests the large B/T are reasonable: these galaxies have large bulges relative to their disks. In fact, NGC 4647 has such a prominent bulge and smooth disk that it is unclear why it was assigned a late RC3 Hubble type : for all intents and purposes it looks like an Sa. The other two (NGC 3810 and 4254) galaxies have prominent bulges and nuclear spiral arms.

How does the bulge Sérsic index n vary as a function of Hubble type, and galaxy stellar mass (Figure 13), as well as B/T, Figure 14 ? Only a small fraction (5.5%) of bulges have classical Sérsic indexes ($n \geq 4$): such bulges lie primarily in S0/a to Sab,and have large

$B/T > 0.2$. A large fraction (34.4%) of bulges have $2 < n < 4$: they exist in barred and unbarred S0/a to Sd, and their B/T spans a wide range with a mean of 0.23. Finally. a striking 60.2% of bulges have $n \leq 2$: they exist in barred and unbarred galaxies across all Hubble types; their B/T spans a wide range (0.01 to 0.4) with a mean of 0.10. In § 5.6, we discuss the possibility that these three types of bulges ($n \geq 4$, $2 < n < 4$, $n \leq 2$) have different formation origins.

5.4. Comparison With Independent Decompositions

As an independent check of our decomposition method, we compare our results with independently published decompositions.

Graham (2001) published $1D$ decompositions for 86 galaxies using optical and near-infrared light profiles. We find our mean H-band B/D (Figure 17) ratios are comparable to his K-band B/D. Like Graham (2001), we find B/D is widely variable with Hubble type and that mean B/D steadily declines from Sa through Scd galaxies. Graham (2001) finds bulge indexes are widely scattered across Hubble type, but they are in general > 1 for early types and < 1 for late types. We likewise find wide scatter in bulge index with $n < 1$ bulges existing in both early and late types.

Another meaningful comparison can be made with Laurikainen et al. (2007) who, using their own $2D$ decomposition code, fit a hybrid sample containing some OSUBSGS galaxies. An important distinction between their work and ours is that they typically model bars with a Ferrers function, but may sometimes use a Sérsic profile, while we only use the latter. Also, they include additional components to model secondary bars or inner disks. They report a distinct offset in the mean B/T between barred and unbarred galaxies, which we confirm in Figure 13. Their mean B/T are similar to ours, and they conclude that pseudobulges exist throughout the Hubble sequence. The Sérsic indexes derived by Laurikainen et al. (2007) are slightly different from ours: there is good agreement in the mean index for barred galaxies, but the indexes of our unbarred galaxies are larger. On the mean, we find unbarred Sa and Sb galaxies to have indexes of ~ 3.25. Laurikainen et al. (2007) find a mean index for unbarred galaxies of the same Hubble types to be ~ 2.25. The discrepancy still exists for Sc-Sd galaxies where our mean indexes are slightly larger by ~ 0.5.

5.5. Comparison of B/T to Hierarchical Models of Galaxy Evolution

For galaxies with stellar mass $M_* \geq 1.0 \times 10^{10} M_\odot$ (where our sample is fairly complete), we plot the cumulative fraction of galaxies with $B/T < x$ as a function of B/T in Figure 19. In the top panel, barred and unbarred galaxies are distinguished, and both populations show an abundance of low-B/T systems. We find that for $M_* \geq 1.0 \times 10^{10} M_\odot$, $\sim 66\%$ spiral galaxies have $B/T \leq 0.2$.

We compare this cumulative fraction with the predictions from cosmological semi-analytical models based on Khochfar & Burkert (2005) and Khochfar & Silk (2006). These models treat the collapse and merging history of dark matter halos separately from the physics of baryons, which govern radiative cooling, star formation, and feedback from supernovae. The merger trees of dark matter halos are calculated according to the prescription in Somerville & Kolatt (1999). The merging history of a halo at z_0 of mass M_0 is reconstructed by recursively tracing the merger histories of the halo's progenitors down to a limiting progenitor mass ($M_{min} \sim 10^9 M_\odot$). Baryonic mass inside the dark matter halos is divided between hot gas, cold gas, and stars. The hot gas is initially shock-heated to the halo virial temperature. As the gas radiatively cools, it settles down into a rotationally supported disk at the halo center. Cold disk gas is allowed to fragment and subsequently form stars according to the Schmidt-Kennicutt law (Kennicutt 1998). Disk star formation is regulated by feedback from supernovae to prevent the formation of too massive satellite galaxies.

During major mergers ($M_1/M_2 \geq 1/4$), disks are destroyed. Cold disk gas is converted to stars, which becomes part of the bulge following violent relaxation of the newly formed and pre-existing stellar mass. As there is mounting numerical evidence (Springel & Hernquist 2005; Cox et al. 2008) that not all not all cold gas is converted to stars, 100% SFE is not assumed. The burst efficiency defined by Cox et al. (2008) is applied to control the fraction of stars formed due to the interaction. This efficiency is dependent on the relative masses of merging galaxies and is expressed as

$$e = e_{1:1} \left(\frac{M_{Satellite}}{M_{Primary}} \right)^{\gamma}, \tag{6}$$

where $e_{1:1}$ is the burst efficiency for a 1:1 merger and γ fixes the dependence on mass ratio; Cox et al. 2008 find $e_{1:1} = 0.55$ and $\gamma = 0.69$.

The remnants of mergers are spheroids with $B/T \sim 1$. Afterward, hot gas in the halo can continue to cool and settle in a disk around the spheroid and make disk stars. In this way B/T grows smaller with time until the next major merger happens, after which B/T is again set ~ 1. Thus, galaxies having their last major merger at high z have small B/T while those with recent last major merger have large B/T (see Figure 18). Between major mergers, the bulge may also grow in mass due to minor mergers, during which the stars in the satellite are added to the bulge of the host. It is important to note that most galaxies fail to experience major mergers. For $M_* \geq 1.0 \times 10^{10} M_\odot$, only about 20% do so. The remaining spirals are built through minor mergers and gas accretion.

Figure 19 shows the comparison between cumulative B/T from the data and the models for $M_* \geq 1.0 \times 10^{10} M_\odot$. The distributions of B/T for real and model galaxies are in close agreement across all B/T. Distinguishing between model galaxies that experienced *both* major and minor mergers from those that experienced *only* minor mergers yields striking results. Galaxies built from both major and minor mergers have mostly $B/T > 0.3$, seriously underpredicting the number of observed low B/T systems. In contrast, those with bulges built from only minor mergers have dominantly $B/T \leq 0.2$ and constitute $\sim$ 60% of all spirals. Table 7 shows the fraction (rather than cumulative fraction) of spirals over different ranges of B/T. It is clear that systems experiencing both major and minor mergers cannot explain the abundance of $B/T \leq 0.2$ systems.

Separating the distribution of B/T by bar class, morphology, and Sérsic index results in curves that lie intermediate between the "Major+Minor" and "Minor Only" lines in Figure 19. The curves for barred galaxies, for Hubble type $Sb \leq T \leq Sc$, and for $n < 2$ lie closer to the latter. This suggests these kinds of systems are less likely to have experienced a major merger. It appears that many of our low B/T systems with $n < 2$ may have had their bulges built mainly from minor mergers and gas accretion. Higher B/T systems with $n > 2$ were likely built from a combination of gas accretion and both major and minor mergers.

Comparison with a model where major mergers are defined to have a larger mass range gives further supports the idea that many low B/T systems are are built from minor mergers. Figure 20 is was calculated identically to Figure 19, except that the condition for disk destruction in mergers has been widened to $M_1/M_2 \geq 1/6$. In this case, the percentage of galaxies experiencing major mergers rises to $\sim$ 30%. There is still good agreement with the data at low B/T, but the model underpredicts the data by about 10% near $B/T = 0.4$. The "Minor Only" curve lies closer to the $Sb \leq T \leq Sc$ and $n < 2$ curves, but it does not match them precisely. This suggests such systems are built from a combination of major and minor mergers, but predominantly by minor mergers with $M_1/M_2 < 1/6$. This is discussed further in §5.6.

5.6. Revisiting Bulge Formation in Hierarchical Models of Galaxy Evolution

Any coherent model of galaxy evolution must explain *both* the distribution of B/T *and* the distribution of Sérsic index (§ 5.3; Figure 13; Figure 19) in our sample of high mass ($M_* \geq 1.0 \times 10^{10} M_\odot$) galaxies. We have shown in §5.5 that models of galaxy evolution agree well with the observed distribution of B/T. We now try to understand the distribution of bulge Sérsic indexes. Only a small fraction (5.5%) of bulges have classical Sérsic indexes ($n \geq 4$). Instead 34.4% have $2 < n < 4$, and 60.2% have $n \leq 2$.

In §5.5 we assume that during major mergers only a fraction of gas is converted to stars before the onset of violent relaxation. The residual dissipative gaseous component will then settle into a disk component whose extent depends on the specific angular momentum distribution of the gas. (1) The gas with high specific angular momentum will form an *extended* gas disk, which later forms a stellar disk *around* the classical bulge. The net effect will be to reduce the amount of mass ending in the classical bulge and in the inner kpc region, thus reducing B/T. (2) Some of the residual gas having low specific angular momentum will likely form a compact gas disk *inside* the classical bulge, later developing into a compact stellar disk with $n \sim$ 1-2 and high V/σ. The latter component is often called a "disky bulge or pseudobulge." We call the combination of a compact stellar disk inside a classical bulge, a *a hybrid bulge with* $2 < n < 4$. The combination of process (1) and (2) would tend to lower *both* the B/T and Sérsic index of bulges.

Several simulations support different aspects of our proposed scenario. Springel et al. (2005) find that in major mergers of very gas-rich spiral galaxies, an extended disk can from gas that is not consumed by SF during the merger and settles into an extended star-forming disk. Robertson et al. (2006) simulate high angular momentum mergers of gas-dominated systems ($M_{\rm gas}/M_{\rm gas+\star}$) > 0.5, that might represent high redshift galaxies. They also find the remnant can be disky or rotationally supported, with the degree of rotational support being determined primarily by feedback processes associated with star formation. Furthermore, ongoing simulations by Hopkins et al (2008, in prep.) of major mergers with mass ratio 1:1 produce different types of ellipticals or bulges depending on the amount of residual gas left over after violent relaxation. The distribution of Sérsic indexes derived by fitting a single Sérsic index to a representative set of 1:1 merger remnants is shown in Figure 21. Note that while $\sim$ 22% of the remnants have classical $n > 4$, as much as 20% have low $n < 2.5$, while 50% have $n < 3$. This suggests that some intermediate $2 < n < 4$ bulges can result from major mergers that have residual gas left-over after violent relaxation.

Based on Figures 19 and 20, most of the bulges with very low $n < 2$ are unlikely to be formed via major mergers of mass ratio 1:1. Some of them form via major mergers of lower mass ratios (e.g. 1:3 or 1:4) where the remnant may be more disky. A significant fraction of them may also form from gas inflows driven by bars and minor mergers at late-epochs: such gas inflows lead to the formation of disky, high V/σ stellar components in the inner kpc, or 'pseudobulges' (Kormendy 1993; Jogee 1999; review by Kormendy & Kennicutt 2004; Jogee, Scoville, & Kenney 2005; Athanassoula 2005). Note that the existence of a low B/T, low $n < 2$ bulge does not imply that the host galaxy has not undergone a major merger; it simply implies that the last major merger occurred at a time when the galaxy was only a small fraction of its present-day mass, such that any high n bulge formed would be subsequently dominated by disky bulges built by later gas inflows driven by bars and minor mergers.

Thus, in summary we suggest the following picture. The *three types of bulges ($n \geq 4$, $2 < n < 4$, $n \leq 2$) likely have different formation origins.* The classical $n \geq 4$ bulges likely form in major mergers which have mass ratios close to 1:1, and where most of the gas gets converted in stars before violent relaxation ends. Conversely, the hybrid $2 < n < 4$ bulges likely form in major mergers that have residual gas left-over after violent relaxation, or in minor mergers. Finally, low $n \leq 2$ bulges likely form from gas inflows driven by bars and minor mergers at late-epochs, and possibly in major or minor mergers of low mass ratios (e.g., 1:3 or lower).

5.7. Bar Strength

Bars are known to exert gravitational torques and drive gas inflows (see §1). Bar strength is an indication of the rate of gas inflow generated due to gravitational torques, which depends on the shape and mass of the bar. Many measures of bar strength have been formulated. The Q_b method of (Block et al. 2002; Buta et al. 2003; Buta et al. 2005) measures directly the gravitational torque at a single point along the bar. This method requires a scaleheight for the disk and a model of the potential to be made from the image. In the bar/interbar contrast method of Elmegreen & Elmegreen (1985) and Elmegreen et al. (1996), bar strength is parameterized as the ratio between peak surface brightness in the bar region and the minimum surface brightness in the interbar region. Elmegreen & Elmegreen (1985) and Elmegreen et al. (1996) also characterize bar strength with the maximum amplitude of the $m = 2$ mode from Fourier decomposition. When ellipse fitting is applied, the maximum ellipticity of the bar, e_{bar}, can be used to characterize bar strength (e.g. MJ07). This constitutes only a partial measure of bar strength, however, as it offers no information about mass or luminosity of the bar.

Bulge-disk-bar decomposition facilitates another evaluation of bar strength with a measure of Bar/T luminosity fraction, which in the H band, traces the stellar mass in the bar.

The upper left panel of Figure 22 plots the individual and mean Bar/T against Hubble type. The spread in Bar/T in each bin is wide, ranging from ~ 0.03 to as high as ~ 0.47. Eight systems have Bar/T near or above 0.3; these are displayed in Figure 23. On the mean, there is a weak tendency for Bar/T to decline down through Sc galaxies, beyond which there are no significant number statistics.

Figures 22 and 24 explore other bar properties and possible correlations with bar strength. Bar Sérsic indexes are mostly below unity. There is no trend in how bar index varies either with Hubble type or with galaxy stellar mass. Bar/T shows no significant trend with galaxy stellar mass or bulge Sérsic index. On the mean, Bar/T rises for bar index less than ~ 0.6, beyond which mean Bar/T is flat. A similar behavior is seen when Bar/T is plotted against bar/bulge luminosity ratio; mean Bar/T rises out to bar/bulge ratio of ~ 4 but is flat at higher ratios. The upper left panel of Figure 24 plots Bar/T against maximum bar ellipticity e_{bar}, as determined by MJ07 for galaxies mutually classified as barred. Not all bars with high e_{bar} have high Bar/T. Rather, there is a spread in Bar/T for a given e_{bar}. The strongest bars, those with high fractional mass and high e_{bar}, should be most effective at driving gas inflows.

5.8. Bar Fraction as Function of B/T and Bulge Index

Bar fraction as a function of B/T and bulge n is worth quantifying as it may have implications on bulge formation scenarios. §5.5 discusses the distribution of B/T and bulge n in our sample. We find three classes of bulge: classical bulges with $n \geq 4$, hybrid bulges with $2 < n < 4$, and pseudobulges with $n \leq 2$. We also find $\sim$ 66% of galaxies have $B/T \leq 0.2$, $\sim$ 31% have $0.2 < B/T < 0.4$, and 11% have $B/T \geq 0.4$.

Table 8 shows how bar fraction varies with bulge class and B/T. Bar fraction declines with bulge index. Pseudobulges have the highest bar fraction (61%). Hybrid bulges have a slightly lower bar fraction (52%). Classical bulges have the lowest bar fraction (29%). Similarly, systems with low B/T are more likely to be barred. For $B/T < 0.2$, the bar fraction is highest (66%). For $0.2 \leq B/T < 0.4$, the bar fraction is almost a factor of two less (38%). $B/T \geq 0.4$ systems have the lowest bar fraction (31%).

These statistics show that bars can account for some of the characteristics of pseudo and hybrid bulges. Pseudobulges can be built from gas inflow driven by bars. Bars can also account to some extent for the disky nature of hybrid bulges. However, not all pseudo or hybrid bulges live in barred systems. This is evidence that minor mergers may play a significant role in bulge assembly.

Systems with classical bulges and high B/T are less likely to contain bars. Such systems are preferentially built by major mergers. As discussed in §5.5, B/T declines over time between major mergers as a disk accretes around the bulge, increasing the total mass in the system. Systems with high B/T may have had fairly recent last major mergers. The likely absence of a bar in such cases can be explained by not enough time elapsing since the last major merger for a bar to be induced in a minor merger or by some other process.

6. Summary

The properties of galaxy components (bulges, disks, and bars) in the local Universe provide key constraints for models of galaxy evolution. Most previous $2D$ decompositions have focused on two-component bulge-disk decomposition, and ignored the contribution of the bar even in strongly barred galaxies. However, as shown by this work and other recent studies (e.g., Laurikainen et al. 2005; Laurikainen et al. 2007; Reese et al. 2007), it is important to include the bar component in the $2D$ decomposition, in order to correctly estimate the bulge-to-total ratio (B/T) and disk properties. In this paper we have developed an iterative $2D$, bulge-disk-bar decomposition technique using GALFIT and applied it to H-band images of $\sim$ 150 moderately inclined spiral galaxies from the OSU Bright Spiral Galaxy Survey. Stellar masses are derived from $B-V$ colors (Figure 4). The sample has primarily spirals with Hubble type S0/a to Sc and stellar mass $M_* \geq 1.0 \times 10^{10} M_\odot$. We performed two-component bulge-disk decomposition, as well as three-component bulge-disk-bar decomposition on the $2D$ light distribution of all galaxies, taking into account the PSF. We use an exponential profile for the disk, and Sérsic profiles for the bulge and bar. A number of quantitative indicators, including bar classification from ellipse fits, are used to pick either the bulge-disk-bar decomposition or bulge-disk decomposition, as the best final fit for a galaxy. Our main results are the following.

1. We find that it is necessary to include the bar component in $2D$ decomposition of barred galaxies, otherwise, the bulge-to-total ratio (B/T) will be overestimated and the disk properties may be skewed. Examples of the effect of including the bar are shown for the prominently barred galaxies NGC 4643 (Figure 6, Table 4) and NGC 4548 (Figure 7, Table 5).

2. We find that out of the 146 moderately inclined spirals ($i \leq 70°$) in our sample, 53.4% are better fit with a Stage 3 bulge-disk-bar decomposition than a Stage 2 bulge-disk decomposition. The resulting H-band bar fraction, defined as the fraction of disk galaxies that are barred, is 58.2%. This fraction is in excellent agreement with the H-

band bar fraction of 60% reported by MJ07, based on ellipse fits of the same sample, with a more conservative inclination cut ($i \leq 60°$).

3. Since we use H-band images, which trace the overall mass fairly well and are not overly impacted by extinction and age gradients, we can use the light fraction of the bulge, disk, and bar (B/T, D/T, Bar/T) as a measure of their mass fraction. For galaxies with $M_* \geq 1.0 \times 10^{10} M_\odot$, we find that 20.4% of stellar mass is in bulges (with 15.7% in $n > 2$ bulges and 4.7% in $n \leq 2$ bulges), 69.6% in disks, and 10.0% in stellar bars.

4. Modeling bars with $2D$ decomposition also allows us to measure bar properties (r_e, n) and the bar-to-total ratio (Bar/T), which is a measure of bar strength. Bar/T spans a wide range, from 0.05 to 0.3 typically, across S0/a to Sc. There is a wide range of Bar/T at each Hubble type. The mean Bar/T declines by 0.1 from S0/a to Sc. (See Figure 22 and Figure 24.)

5. We explore the relationship between B/T, bulge Sérsic index, and Hubble types (Figure 13). Only a small fraction (5.5%) of bulges have classical Sérsic indexes ($n \geq 4$): such bulges lie primarily in S0/a to Sab, and have large $B/T > 0.2$. A large fraction (34.4%) of bulges have $2 < n < 4$: they exist in barred and unbarred S0/a to Sd, and their B/T spans a wide range (0.03 to 0.5) with a mean of 0.23. Finally, a striking 60.2% of bulges have $n \leq 2$: they exist in barred and unbarred galaxies across all Hubble types; their B/T spans a wide range (0.01 to 0.4) with a mean of 0.10. We suggest that these three types of bulges ($n \geq 4$, $2 < n < 4$, $n \leq 2$) may have different formation origins (see point 7).

6. From the distribution of B/T (Figure 13), we find the following. Bulges with very high B/T (> 0.4) exist primarily in galaxies with high mass ($M_* > 6 \times 10^{10} M_\odot$) and early types (S0/a to Sab). Bulges with very low B/T (< 0.1) lie primarily in lower mass galaxies with later morphologies (Sb to Sc). However, it is striking that bulges with $B/T \leq 0.2$ are pervasive and exist across the whole spectrum of S0/a to Scd.

7. We explore the cumulative fraction of galaxies as a function of B/T (Figure 19) and compare it to predictions from ΛCDM cosmological semi-analytic models of galaxy evolution, which assume that every major merger of mass ratio above 4:1 results in a bulge. For $M_* \geq 2.5 \times 10^{10} M_\odot$, $\sim 66\%$ of spiral galaxies have $B/T \leq 0.2$. The distribution in B/T of spirals with bulges built by major mergers sersiously underpredicts the observed abundance of low B/T systems. Most galaxies in the models experience only minor mergers, and on the whole ΛCDM-based models agree well with the data provided almost all $B/T < 0.2$ systems are built from minor mergers.

8. We revisit bulge formation in hierarchical models of galaxy evolution, with the idea that any correct model must explain *both* the distribution of B/T *and* the distribution of Sérsic index (Figure 13 and Figure 19) in our sample of high mass ($M_* \geq 1.0 \times 10^{10} M_\odot$) galaxies. Not only do $\sim 66\%$ bulges have low $B/T < 0.2$, but in addition 34.4% have $2 < n < 4$, and 60.2% have $n \leq 2$. We suggest that the *three types of bulges ($n \geq 4$, $2 < n < 4$, $n \leq 2$) likely have different formation origins.* The classical $n \geq 4$ bulges likely form in major mergers which have mass ratios close to 1:1, and where most of the gas gets converted in stars before violent relaxation ends. Conversely, the hybrid $2 < n < 4$ bulges likely form in major mergers that have residual gas left-over after violent relaxation, or in minor mergers. Finally, low $n \leq 2$ bulges likely form from gas inflows driven by bars and minor mergers at late-epochs, and possibly in major or minor mergers of low mass ratios (e.g., 1:3 or lower).

We acknowledge technical assistance from Chien Peng in the operation of GALFIT. We thank John Kormendy and Karl Gebhardt for helpful constructive criticism. We acknowledge the usage of the Hyperleda database (http://leda.univ-lyon1.fr). This research has made use of the NASA/IPAC Extragalactic Database (NED) which is operated by the Jet Propulsion Laboratory, California Institute of Technology, under contract with the National Aeronautics and Space Administration.

REFERENCES

Allen, P. D., Driver, S. P., Graham, A. W., Cameron, E., Liske, J., & de Propris, R. 2006, MNRAS, 371, 2

Athanassoula, E. 2002, ApJL, 569, L83

Athanassoula, E. 2003, MNRAS, 341, 1179

Athanassoula, E. 2005, MNRAS, 358, 1477

Barazza, F. D., Jogee, S., & Marinova, I. 2007, IAU Symposium, 235, 76

Barazza, F. D., Jogee, S., & Marinova, I. 2008, ApJ, 675, 1194

Barrett, P. E., & Bridgman, W. T. 1999, Astronomical Data Analysis Software and Systems VIII, 172, 483

Bell, E. F., McIntosh, D. H., Katz, N., & Weinberg, M. D. 2003, ApJS, 149, 289

Berentzen, I., Shlosman, I., & Jogee, S. 2006, ApJ, 637, 582

Blanton, M. R., Lupton, R. H., Schlegel, D. J., Strauss, M. A., Brinkmann, J., Fukugita, M., & Loveday, J. 2005, ApJ, 631, 208

Block, D. L., Bournaud, F., Combes, F., Puerari, I., & Buta, R. 2002, A&A, 394, L35

Böker, T., Laine, S., van der Marel, R. P., Sarzi, M., Rix, H.-W., Ho, L. C., & Shields, J. C. 2002, AJ, 123, 1389

Burkert, A., & Naab, T. 2004, Coevolution of Black Holes and Galaxies, 421

Burkert, A. M., & D'Onghia, E. 2004, Penetrating Bars Through Masks of Cosmic Dust, 319, 341

Buta, R., Block, D. L., & Knapen, J. H. 2003, AJ, 126, 1148

Buta, R., Vasylyev, S., Salo, H., & Laurikainen, E. 2005, AJ, 130, 506

Byun, Y. I., & Freeman, K. C. 1995, ApJ, 448, 563

Charlot, S., Worthey, G., & Bressan, A. 1996, ApJ, 457, 625

Cole, S., Lacey, C. G., Baugh, C. M., & Frenk, C. S. 2000, MNRAS, 319, 168

Cox, T. J., Jonsson, P., Somerville, R. S., Primack, J. R., & Dekel, A. 2008, MNRAS, 384, 386

Debattista, V. P., & Sellwood, J. A. 1998, ApJL, 493, L5

de Jong, R. S. 1996, A&A Suppl., 118, 557

de Souza, R. E., Gadotti, D. A., & dos Anjos, S. 2004, ApJS, 153, 411

de Vaucouleurs, G., de Vaucouleurs, A., Corwin, H. G., Jr., Buta, R. J., Paturel, G., & Fouque, P. 1991, Volume 1-3, XII, 2069 pp. 7 figs.. Springer-Verlag Berlin Heidelberg New York,

D'Onghia, E., Burkert, A., Murante, G., & Khochfar, S. 2006, MNRAS, 372, 1525

Driver, S. P., Liske, J., Cross, N. J. G., De Propris, R., & Allen, P. D. 2005, MNRAS, 360, 81

Efstathiou, G., Ellis, R. S., & Peterson, B. A. 1988, MNRAS, 232, 431

Elmegreen, B. G., & Elmegreen, D. M. 1985, ApJ, 288, 438

Elmegreen, B. G. 1994, ApJL, 425, L73

Elmegreen, B. G., Elmegreen, D. M., Chromey, F. R., Hasselbacher, D. A., & Bissell, B. A. 1996, AJ, 111, 2233

Eskridge, P. B., et al. 2000, AJ, 119, 536

Eskridge, P. B., et al. 2002, ApJS, 143, 73

Gadotti, D., & Kauffmann, G. 2007, IAU Symposium, 241, 507

Graham, A. W. 2001, AJ, 121, 820

Ho, L. C., Filippenko, A. V., & Sargent, W. L. W. 1997, ApJS, 112, 315

Hunt, L. K., & Malkan, M. A. 1999, ApJ, 516, 660

Jogee, S. 1999, Ph.D. Thesis,

Jogee, S., Kenney, J. D. P., & Smith, B. J. 1999, ApJ, 526, 665

Jogee, S., et al. 2004, ApJL, 615, L105

Jogee, S., Scoville, N., & Kenney, J. D. P. 2005, ApJ, 630, 837

Jogee, S. 2006, Physics of Active Galactic Nuclei at all Scales, 693, 143

Jogee, S., et al. 2008, ArXiv e-prints, 802, arXiv:0802.3901

Kautsch, S. J., Grebel, E. K., Barazza, F. D., & Gallagher, J. S., III 2006, A&A, 445, 765

Kennicutt, R. C., Jr. 1998, ApJ, 498, 541

Khochfar, S., & Burkert, A. 2005, MNRAS, 359, 1379

Khochfar, S., & Silk, J. 2006, MNRAS, 370, 902

Knapen, J. H., Beckman, J. E., Heller, C. H., Shlosman, I., & de Jong, R. S. 1995, ApJ, 454, 623

Knapen, J. H., Shlosman, I., & Peletier, R. F. 2000, ApJ, 529, 93

Kormendy, J. 1993, Galactic Bulges, 153, 209

Kormendy, J., & Kennicutt, R. C., Jr. 2004, ARAA, 42, 603

Kormendy, J., & Fisher, D. B. 2005, Rev. Mex. A&A (Conferencias), 23, 101 (astro-ph/0507525)

Kormendy, J. 2007, in IAU Symposium 245, Formation and Evolution of Galaxy Bulges, ed. M. Bureau et al. (Cambridge Univ. Press), in press (astro-ph 0708.2104)

Kormendy, J. 2008, Rome paper. (Placeholder)

Kroupa, P., Tout, C. A., & Gilmore, G. 1993, MNRAS, 262, 545

Laine, S., Shlosman, I., Knapen, J. H., & Peletier, R. F. 2002, ApJ, 567, 97

Laurikainen, E., Salo, H., Buta, R., & Vasylyev, S. 2004, MNRAS, 355, 1251

Laurikainen, E., Salo, H., & Buta, R. 2004, ApJ, 607, 103

Laurikainen, E., Salo, H., & Buta, R. 2005, MNRAS, 362, 1319

Laurikainen, E., Salo, H., Buta, R., & Knapen, J. H. 2007, MNRAS, 381, 401 & Block, D. 2006, AJ, 132, 2634

Liske, J., Lemon, D. J., Driver, S. P., Cross, N. J. G., & Couch, W. J. 2003, MNRAS, 344, 307

Marinova, I., & Jogee, S. 2007, ApJ, 659, 1176

Mulchaey, J. S., & Regan, M. W. 1997, ApJL, 482, L135

Naab, T., & Burkert, A. 2001, ApJL, 555, L91

Paturel G., Petit C., Prugniel P., Theureau G., Rousseau J., Brouty M., Dubois P., Cambrésy L., 2003, A&A, 412, 45

Peng, C. Y., Ho, L. C., Impey, C. D., & Rix, H.-W. 2002, AJ, 124, 266

Reese, A. S., Williams, T. B., Sellwood, J. A., Barnes, E. I., & Powell, B. A. 2007, AJ, 133, 2846

Robertson, B., Yoshida, N., Springel, V., & Hernquist, L. 2004, ApJ, 606, 32

Robertson, B., Bullock, J. S., Cox, T. J., Di Matteo, T., Hernquist, L., Springel, V., & Yoshida, N. 2006, ApJ, 645, 986

Sheth, K., et al. 2008, ApJ, 675, 1141

Simard, L. 1998, Astronomical Data Analysis Software and Systems VII, 145, 108

Simard, L., et al. 2002, ApJS, 142, 1

Somerville, R. S., & Kolatt, T. S. 1999, MNRAS, 305, 1

Springel, V., & Hernquist, L. 2005, ApJL, 622, L9

Springel, V., Di Matteo, T., & Hernquist, L. 2005, MNRAS, 361, 776

Steinmetz, M., & Navarro, J. F. 2002, New Astronomy, 7, 155

Véron-Cetty, M.-P., & Véron, P. 2006, A&A, 455, 773

Wadadekar, Y., Robbason, B., & Kembhavi, A. 1999, AJ, 117, 1219

Warren, S. J., et al. 2007, MNRAS, 375, 213

Weinberg, M. D. 1985, MNRAS, 213, 451

Table 1. OSUBSGS Galaxies (N=146)

Galaxy Name (1)	Hubble Type (RC3) (2)	Bar Type (RC3) (3)	D (Mpc) (4)	M_B (mag) (5)	$B-V$ (mag) (6)	M_* ($M_\odot$) (7)
ESO138-10	SA(s)cd	A	16.35	-	-	-
IC0239	SAB(rs)cd	AB	12.91	-19.10	0.70	1.34e+10
IC4444	SAB(rs)bc	AB	27.83	-20.23	0.64	4.35e+10
IC5325	SAB(rs)bc	AB	21.40	-19.83	0.56	9.78e+09
NGC0150	SB(rs)bc	B	21.76	-19.70	0.64	2.17e+10
NGC0157	SAB(rs)bc	AB	24.72	-20.97	0.59	5.81e+10
NGC0210	SAB(s)b	AB	24.78	-20.38	0.71	3.77e+10
NGC0278	SAB(rs)b	AB	8.88	-18.27	0.64	1.24e+10
NGC0289	SAB(rs)bc	AB	24.14	-20.20	0.73	3.33e+10
NGC0428	SAB(s)m	AB	14.93	-18.96	0.44	5.28e+09
NGC0488	SA(r)b	A	31.90	-21.38	0.87	2.44e+11
NGC0578	SAB(rs)c	AB	22.81	-20.36	0.51	1.87e+10
NGC0613	SB(rs)bc	B	21.57	-20.95	0.68	4.92e+10
NGC0685	SAB(r)c	AB	21.57	-19.96	0.46	5.47e+09
NGC0779	SAB(r)b	AB	20.33	-19.60	0.79	3.64e+10
NGC0864	SAB(rs)c	AB	22.14	-20.33	0.55	2.31e+10
NGC0908	SA(s)c	A	24.30	-21.11	0.65	6.60e+10
NGC1042	SAB(rs)cd	AB	20.10	-19.96	0.54	1.63e+10
NGC1058	SA(rs)c	A	7.03	-17.42	0.62	4.74e+09
NGC1073	SB(rs)c	B	17.27	-19.72	0.50	1.04e+10
NGC1084	SA(s)c	A	20.20	-20.22	0.58	2.64e+10
NGC1087	SAB(rs)c	AB	20.20	-20.21	0.52	2.09e+10
NGC1187	SB(r)c	B	22.08	-20.39	0.56	1.66e+10
NGC1241	SB(rs)b	B	56.27	-21.78	0.85	2.05e+11
NGC1300	SB(rs)bc	B	22.74	-20.68	0.68	5.39e+10
NGC1302	(R)SB(r)0	B	24.72	-20.37	0.89	6.37e+10
NGC1309	SA(s)bc	A	32.24	-20.58	0.44	1.46e+10
NGC1317	SAB(r)a	AB	27.73	-20.31	0.89	6.42e+10
NGC1350	(R')SB(r)ab	B	26.52	-20.97	0.87	1.38e+11
NGC1371	SAB(rs)a	AB	20.77	-	-	-
NGC1385	SB(s)cd	B	20.77	-20.82	0.51	1.61e+10
NGC1511	SAa;pec	A	19.06	-19.53	0.57	1.15e+10
NGC1559	SB(s)cd	B	19.06	-20.41	0.35	9.33e+09
NGC1637	SAB(rs)c	AB	10.14	-18.56	0.64	4.70e+09
NGC1703	SB(r)b	B	21.80	-19.80	0.56	8.43e+09
NGC1792	SA(rs)bc	A	17.40	-20.34	0.68	3.71e+10
NGC1808	(R)SAB(s)a	AB	14.49	-20.07	0.81	3.57e+10
NGC1964	SAB(s)b	AB	24.27	-20.35	0.77	6.54e+10
NGC2090	SA(rs)c	A	13.17	-19.15	0.79	1.90e+10
NGC2139	SAB(rs)cd	AB	26.11	-20.10	0.36	8.35e+09
NGC2196	(R')SA(s)a	A	32.87	-20.77	0.81	9.22e+10
NGC2442	SAB(s)bc;pec	AB	19.98	-20.27	0.82	8.28e+10
NGC2559	SB(s)bc;pec	B	22.29	-	-	-
NGC2566	(R')SB(rs)ab;pec	B	23.40	-21.75	0.81	6.98e+10
NGC2775	SA(r)ab	A	19.14	-20.39	0.90	9.46e+10
NGC3059	SB(rs)c	B	19.14	-19.64	0.68	2.52e+10

Table 1—Continued

Galaxy Name (1)	Hubble Type (RC3) (2)	Bar Type (RC3) (3)	D (Mpc) (4)	M_B (mag) (5)	$B-V$ (mag) (6)	M_* ($M_\odot$) (7)
NGC3166	SAB(rs)0	AB	18.94	-20.07	0.93	7.41e+10
NGC3169	SA(s)a;pec	A	18.01	-20.20	0.85	6.09e+10
NGC3223	SA(s)b	A	41.23	-21.30	0.82	2.36e+11
NGC3227	SAB(s)a;pec	AB	18.89	-19.97	0.82	4.42e+10
NGC3261	SB(rs)b	B	36.64	-	-	-
NGC3275	SB(r)ab	B	45.87	-	-	-
NGC3319	SB(rs)cd	B	45.87	-18.73	0.41	4.76e+09
NGC3338	SA(s)c	A	18.53	-19.70	0.59	2.67e+10
NGC3423	SA(s)cd	A	11.93	-18.80	0.45	5.89e+09
NGC3504	(R)SAB(s)ab	AB	21.69	-19.87	0.72	4.06e+10
NGC3513	SB(rs)c	B	17.00	-19.23	0.43	7.52e+09
NGC3583	SB(s)b	B	30.54	-	-	-
NGC3596	SAB(rs)c	AB	16.80	-	-	-
NGC3646	Ring	-	60.87	-22.16	0.65	2.82e+11
NGC3675	SA(s)b	A	10.34	-	-	-
NGC3684	SA(rs)bc	A	19.92	-19.50	0.62	1.00e+10
NGC3686	SB(s)bc	B	14.76	-18.96	0.57	9.97e+09
NGC3705	SAB(r)ab	AB	15.06	-19.03	0.79	3.15e+10
NGC3726	SAB(r)c	AB	13.54	-19.75	0.49	1.93e+10
NGC3810	SA(rs)c	A	13.68	-19.34	0.58	1.72e+10
NGC3885	SA(s)0	A	27.40	-20.31	0.95	4.62e+10
NGC3887	SB(r)bc	B	17.27	-	-	-
NGC3893	SAB(rs)c	AB	13.49	-	-	-
NGC3938	SA(s)c	A	11.01	-19.31	0.52	1.23e+10
NGC3949	SA(s)bc	AB	9.73	-18.40	0.45	8.66e+09
NGC4027	SB(s)dm	B	9.73	-20.20	0.54	2.25e+10
NGC4030	SA(s)bc	A	20.94	-	-	-
NGC4051	SAB(rs)bc	AB	9.83	-19.14	0.65	1.95e+10
NGC4062	SA(s)c	A	10.60	-18.23	0.76	2.07e+10
NGC4123	SB(r)c	B	17.69	-19.26	0.61	1.50e+10
NGC4145	SAB(rs)d	AB	13.21	-18.83	0.51	1.34e+10
NGC4151	(R')SAB(rs)ab	AB	13.66	-19.18	0.73	2.93e+10
NGC4212	SAc	A	1.16	-13.48	0.67	3.28e+10
NGC4254	SA(s)c	A	34.41	-22.25	0.57	1.61e+11
NGC4293	(R)SB(s)0	B	10.24	-18.80	0.90	5.94e+10
NGC4303	SAB(rs)bc	AB	22.96	-21.63	0.53	6.76e+10
NGC4314	SB(rs)a	B	13.76	-19.27	0.85	3.69e+10
NGC4394	(R)SB(r)b	B	11.03	-18.48	0.85	2.61e+10
NGC4414	SA(rs)c	A	10.23	-19.09	0.84	4.38e+10
NGC4450	SA(s)ab	A	27.93	-21.49	0.82	2.22e+11
NGC4487	SAB(rs)cd	AB	14.78	-	-	-
NGC4490	SB(s)d;pec	B	8.49	-19.43	0.43	4.10e+10
NGC4527	SAB(s)bc	AB	24.67	-20.59	0.86	1.87e+11
NGC4548	SB(rs)b	B	6.95	-18.42	0.81	7.85e+10
NGC4593	(R)SB(rs)b	B	38.57	-	-	-
NGC4618	SB(rs)m	B	38.57	-18.23	0.44	4.62e+09

Table 1—Continued

Galaxy Name (1)	Hubble Type (RC3) (2)	Bar Type (RC3) (3)	D (Mpc) (4)	M_B (mag) (5)	$B-V$ (mag) (6)	M_* ($M_\odot$) (7)
NGC4643	SB(rs)0	B	19.98	-19.79	0.96	6.49e+10
NGC4647	SAB(rs)c	AB	20.30	-19.60	0.65	1.67e+10
NGC4651	SA(rs)c	A	11.26	-18.87	0.57	1.05e+10
NGC4654	SAB(rs)cd	AB	14.95	-20.13	0.60	2.99e+10
NGC4665	SB(s)0	B	11.22	-	-	-
NGC4689	SA(rs)bc	A	21.74	-20.09	0.65	3.84e+10
NGC4691	(R)SB(s)0;pec	B	15.83	-19.34	0.58	1.04e+10
NGC4698	SA(s)ab	A	14.74	-19.39	0.91	5.15e+10
NGC4699	SAB(rs)b	AB	21.12	-21.22	0.89	2.06e+11
NGC4772	SA(s)a	A	14.87	-18.91	0.92	3.30e+10
NGC4775	SA(s)d	A	22.41	-	-	-
NGC4781	SB(rs)d	B	18.01	-	-	-
NGC4818	SAB(rs)ab;pec	AB	15.36	-18.94	0.89	3.88e+10
NGC4856	SB(s)0	B	17.87	-19.78	0.99	9.04e+10
NGC4902	SB(r)b	B	38.93	-21.36	0.69	8.33e+10
NGC4930	SB(rs)b	B	36.73	-20.84	0.90	1.61e+11
NGC4939	SA(s)bc	A	44.16	-21.34	0.64	1.43e+11
NGC4941	(R)SAB(r)ab	AB	12.09	-18.52	0.84	2.50e+10
NGC4995	SAB(rs)b	AB	24.90	-20.39	0.87	8.25e+10
NGC5054	SA(s)bc	A	25.59	-20.38	0.76	8.31e+10
NGC5085	SA(s)c	A	27.96	-20.67	0.87	2.54e+10
NGC5101	(R)SB(rs)0	B	26.28	-20.48	1.00	1.69e+11
NGC5121	(R')SA(s)a	A	21.46	-20.16	0.95	3.68e+10
NGC5161	SA(s)c	A	34.32	-20.69	0.79	1.65e+11
NGC5247	SA(s)bc	A	19.51	-20.96	0.54	3.86e+10
NGC5371	SAB(rs)bc	AB	36.78	-21.52	0.70	1.74e+11
NGC5427	SA(s)c;pec	A	19.51	-20.97	0.57	4.61e+10
NGC5483	SA(s)c	A	25.32	-	-	-
NGC5643	SAB(rs)c	AB	16.62	-20.37	0.74	6.68e+10
NGC5676	SA(rs)bc	A	30.59	-20.57	0.68	9.01e+10
NGC5701	(R)SB(rs)0	B	22.23	-19.98	0.88	4.67e+10
NGC5713	SAB(rs)bc;pec	AB	26.90	-20.32	0.64	5.21e+10
NGC5850	SB(r)b	B	35.47	-21.22	0.79	1.37e+11
NGC5921	SB(r)bc	B	20.82	-20.11	0.66	3.51e+10
NGC5962	SA(r)c	A	28.47	-20.30	0.64	4.43e+10
NGC6215	SA(s)c	A	21.73	-19.69	0.54	1.84e+10
NGC6221	SB(s)bc;pec	B	19.29	-20.77	0.74	1.31e+11
NGC6300	SB(rs)b	B	15.85	-20.81	0.78	4.49e+10
NGC6384	SAB(r)bc	AB	24.14	-20.78	0.72	1.05e+11
NGC6753	(R)SA(r)b	A	44.88	-21.31	0.83	1.81e+11
NGC6782	(R)SAB(r)a	AB	55.60	-	-	-
NGC6902	SA(r)b	A	39.97	-21.44	0.71	8.12e+10
NGC6907	SB(s)bc	B	44.64	-21.36	0.69	1.21e+11
NGC7083	SA(s)bc	A	43.70	-21.35	0.65	1.05e+11
NGC7205	SA(s)bc	A	21.17	-20.09	0.60	3.11e+10
NGC7213	SA(s)a	A	25.76	-21.05	0.89	1.26e+11

Table 1—Continued

Galaxy Name (1)	Hubble Type (RC3) (2)	Bar Type (RC3) (3)	D (Mpc) (4)	M_B (mag) (5)	$B-V$ (mag) (6)	M_* ($M_\odot$) (7)
NGC7217	(R)SA(r)ab	A	13.36	-19.61	0.90	8.38e+10
NGC7412	SB(s)b	B	24.51	-20.07	0.53	1.50e+10
NGC7479	SB(s)c	B	34.20	-21.08	0.75	1.44e+11
NGC7552	(R')SB(s)ab	B	23.61	-20.62	0.68	3.49e+10
NGC7723	SB(r)b	B	27.07	-20.23	0.73	4.32e+10
NGC7727	SAB(s)a;pec	AB	26.23	-20.60	0.91	1.13e+11
NGC7741	SB(s)cd	B	10.79	-18.33	0.53	6.67e+09
NGC7814	SA(s)ab;sp	AB	14.88	-19.31	0.99	8.02e+10

Note. — Columns are : (1) Galaxy name. (2) Hubble type from RC3 (de Vaucouleurs et al. 1991). (3) RC3 bar type, which is based on visual inspection of optical images and runs as 'B'='strongly barred', 'AB'='weakly barred', and 'A'='unbarred'. (4) Distance in Mpc calculated assuming a Hubble constant of 70 km s^{-1} Mpc^{-1}. (5) Extinction and k-corrected absolute B-band magnitude from Hyperleda. (6) $B-V$ color from Hyperleda. (7) Stellar mass, calculated as outlined in §2.2.

Table 2. Structural Parameters of 146 OSUBSGS Galaxies

Galaxy Name	Best Fit	B/T (%)	D/T (%)	Bar/T (%)	Bulge r_e (")	Bulge r_e (kpc)	Bulge n	Disk h (")	Disk h (kpc)	Bar r_e (")	Bar r_e (kpc)	Bar n
(1)	(2)	(3)	(4)	(5)	(6)	(7)	(8)	(9)	(10)	(11)	(12)	(13)
ESO138-10	PSF+Bulge+Disk	16.30	83.70	0.00	10.94	0.86	2.07	27.10	2.14	-	-	-
IC0239	Bulge+Disk+Bar	2.75	92.70	4.52	6.38	0.40	0.61	34.59	2.16	14.23	0.89	0.17
IC4444	Bulge+Disk	32.00	68.00	0.00	7.94	1.06	2.33	17.67	2.36	-	-	-
IC5325	PSF+Bulge+Disk	6.79	93.20	0.00	15.17	1.56	1.75	23.18	2.39	-	-	-
NGC0150	PSF+Bulge+Disk+Bar	5.72	81.20	13.10	4.22	0.44	0.05	33.57	3.52	17.82	1.87	0.39
NGC0157	Bulge+Disk	2.30	97.70	0.00	1.71	0.20	1.76	31.77	3.78	-	-	-
NGC0210	Bulge+Disk+Bar	30.10	48.50	21.40	4.81	0.57	1.71	83.21	9.92	29.41	3.51	0.31
NGC0278	Bulge+Disk	4.41	95.60	0.00	2.77	0.12	1.43	13.48	0.58	-	-	-
NGC0289	Bulge+Disk+Bar	6.45	88.20	5.32	4.79	0.56	0.54	20.28	2.36	16.87	1.96	0.05
NGC0428	Bulge+Disk+Bar	5.38	71.60	23.10	9.00	0.65	0.59	32.46	2.34	30.51	2.20	0.40
NGC0488	Bulge+Disk	21.90	78.10	0.00	9.91	1.52	3.24	38.69	5.92	-	-	-
NGC0578	PSF+Bulge+Disk+Bar	2.05	93.60	4.32	4.19	0.46	0.56	40.73	4.47	14.95	1.64	0.18
NGC0613	Bulge+Disk+Bar	13.90	56.80	29.30	6.28	0.65	1.41	45.79	4.76	63.66	6.61	0.52
NGC0685	Bar+Disk	0.00	96.50	3.47	-	-	-	41.24	4.28	20.68	2.15	0.16
NGC0779	Bulge+Disk+Bar	16.20	57.70	26.10	6.04	0.59	2.31	38.74	3.79	29.00	2.84	0.25
NGC0864	PSF+Bulge+Disk+Bar	2.77	86.90	10.30	3.52	0.38	0.66	39.54	4.22	21.07	2.25	0.37
NGC0908	PSF+Bulge+Disk	8.86	91.10	0.00	7.18	0.84	1.62	48.96	5.72	-	-	-
NGC1042	PSF+Bulge+Disk	2.88	97.10	0.00	6.17	0.60	0.17	43.94	4.25	-	-	-
NGC1058	PSF+Bulge+Disk	1.90	98.10	0.00	1.73	0.06	0.30	21.36	0.73	-	-	-
NGC1073	PSF+Bulge+Disk+Bar	2.36	79.60	18.10	5.47	0.46	0.41	50.02	4.17	34.24	2.85	0.83
NGC1084	PSF+Bulge+Disk	5.23	94.80	0.00	3.24	0.32	0.77	18.68	1.82	-	-	-
NGC1087	Bar+Disk	0.00	93.10	6.87	-	-	-	28.55	2.78	7.79	0.76	1.27
NGC1187	PSF+Bulge+Disk+Bar	6.94	65.00	28.10	4.81	0.51	1.57	38.20	4.06	51.85	5.51	0.72
NGC1241	Bulge+Disk+Bar	11.70	68.50	19.80	2.21	0.59	1.25	27.77	7.45	17.98	4.83	0.52
NGC1300	Bulge+Disk+Bar	12.70	74.20	13.10	4.83	0.53	2.43	65.51	7.17	69.62	7.62	0.25
NGC1302	PSF+Bulge+Disk+Bar	17.60	63.80	18.60	4.96	0.59	2.01	44.92	5.34	20.44	2.43	0.76
NGC1309	Bulge+Disk	31.00	69.00	0.00	13.36	2.07	3.02	15.97	2.47	-	-	-
NGC1317	Bulge+Disk+Bar	13.90	41.50	44.70	3.99	0.53	1.94	47.37	6.31	20.22	2.69	2.19
NGC1350	Bulge+Disk+Bar	24.90	67.50	7.60	9.80	1.25	3.05	56.17	7.16	46.90	5.98	0.18
NGC1371	Bulge+Disk+Bar	14.90	77.30	7.87	5.93	0.59	2.90	30.95	3.10	17.14	1.72	0.51
NGC1385	Bar+Disk	0.00	75.80	24.20	-	-	-	27.65	2.77	16.07	1.61	1.45
NGC1511	Bulge+Disk	28.50	71.50	0.00	27.78	2.55	1.35	23.99	2.20	-	-	-
NGC1559	Bar+Disk	0.00	97.00	3.01	-	-	-	31.17	2.86	9.56	0.88	0.71
NGC1637	PSF+Bulge+Disk+Bar	5.85	90.30	3.84	4.42	0.22	0.59	39.00	1.91	15.45	0.76	0.15

Table 2—Continued

Galaxy Name	Best Fit	B/T (%)	D/T (%)	Bar/T (%)	Bulge r_e (")	Bulge r_e (kpc)	Bulge n	Disk h (")	Disk h (kpc)	Bar r_e (")	Bar r_e (kpc)	Bar n
(1)	(2)	(3)	(4)	(5)	(6)	(7)	(8)	(9)	(10)	(11)	(12)	(13)
NGC1703	Bulge+Disk	6.81	93.20	0.00	2.49	0.26	1.33	18.63	1.96	-	-	-
NGC1792	Bulge+Disk	2.73	97.30	0.00	3.27	0.27	1.40	38.59	3.24	-	-	-
NGC1808	Bulge+Disk+Bar	3.97	74.20	21.80	2.42	0.17	0.69	38.73	2.71	5.70	0.40	0.67
NGC1964	PSF+Bulge+Disk+Bar	41.80	49.90	8.35	8.31	0.97	2.58	18.59	2.17	8.05	0.94	0.05
NGC2090	Bulge+Disk+Bar	14.70	58.40	26.90	17.68	1.12	2.19	160.02	10.17	33.74	2.14	0.43
NGC2139	Bulge+Disk	15.20	84.80	0.00	8.27	1.04	1.53	18.12	2.27	-	-	-
NGC2196	PSF+Bulge+Disk	46.40	53.60	0.00	13.42	2.12	2.38	28.38	4.48	-	-	-
NGC2442	Bulge+Disk+Bar	13.70	62.20	24.10	4.76	0.46	2.04	79.74	7.68	60.42	5.82	0.23
NGC2559	Bulge+Disk+Bar	6.98	81.60	11.40	4.01	0.43	1.38	34.65	3.72	21.40	2.30	0.24
NGC2566	Bulge+Disk	22.70	77.30	0.00	1.74	0.20	4.42	23.05	2.60	-	-	-
NGC2775	PSF+Bulge+Disk	60.90	39.10	0.00	47.35	4.37	4.85	28.09	2.59	-	-	-
NGC3059	Bar+Disk	0.00	90.70	9.32	-	-	-	64.22	5.92	23.94	2.21	1.43
NGC3166	Bulge+Disk+Bar	25.00	50.70	24.30	3.25	0.30	0.81	20.14	1.84	13.85	1.26	0.53
NGC3169	Bulge+Disk	50.90	49.10	0.00	17.46	1.52	4.16	68.70	5.96	-	-	-
NGC3223	Bulge+Disk	14.80	85.20	0.00	6.94	1.37	2.98	29.90	5.90	-	-	-
NGC3227	PSF+Bulge+Disk+Bar	10.80	45.20	44.00	4.84	0.44	0.32	44.67	4.07	39.51	3.60	1.27
NGC3261	Bulge+Disk+Bar	15.20	70.00	14.80	2.87	0.51	2.21	29.07	5.11	14.00	2.46	1.05
NGC3275	Bulge+Disk+Bar	14.30	63.40	22.40	2.19	0.48	1.93	28.27	6.20	20.77	4.56	0.95
NGC3319	Bar+Disk	0.00	94.40	5.63	-	-	-	66.08	14.49	14.11	3.09	0.47
NGC3338	PSF+Bulge+Disk+Bar	5.29	82.00	12.80	4.39	0.39	0.76	36.42	3.25	20.62	1.84	0.39
NGC3423	Bulge+Disk	28.10	71.90	0.00	24.09	1.39	2.39	31.21	1.80	-	-	-
NGC3504	Bulge+Disk+Bar	23.10	39.50	37.40	2.37	0.25	1.04	29.55	3.09	26.02	2.72	0.78
NGC3513	Bulge+Disk+Bar	4.45	92.10	3.47	10.73	0.88	1.46	33.18	2.72	18.32	1.50	0.08
NGC3583	Bulge+Disk+Bar	8.62	53.40	38.00	1.29	0.19	1.28	21.78	3.19	14.89	2.18	0.68
NGC3596	PSF+Bulge+Disk	12.10	87.90	0.00	5.34	0.43	0.67	18.54	1.50	-	-	-
NGC3646	PSF+Bulge+Disk	13.50	86.50	0.00	3.60	1.04	1.20	26.01	7.54	-	-	-
NGC3675	PSF+Bulge+Disk	44.40	55.60	0.00	28.41	1.42	2.66	47.12	2.35	-	-	-
NGC3684	Bulge+Disk	22.90	77.10	0.00	9.95	0.95	2.45	15.66	1.50	-	-	-
NGC3686	Bulge+Disk+Bar	3.23	94.80	1.93	3.10	0.22	2.39	27.59	1.96	16.65	1.19	0.06
NGC3705	Bulge+Disk+Bar	29.40	57.60	13.10	9.09	0.66	2.29	37.70	2.74	30.06	2.18	0.07
NGC3726	Bulge+Disk+Bar	3.60	94.70	1.66	5.08	0.33	2.73	49.95	3.26	48.81	3.19	0.03
NGC3810	PSF+Bulge+Disk	38.40	61.60	0.00	12.35	0.82	1.28	23.78	1.57	-	-	-
NGC3885	PSF+Bulge+Disk	27.10	72.90	0.00	3.13	0.41	0.46	11.94	1.57	-	-	-
NGC3887	Bulge+Disk+Bar	3.36	82.80	13.90	3.81	0.32	1.74	40.52	3.37	39.41	3.28	1.11

Table 2—Continued

Galaxy Name	Best Fit	B/T (%)	D/T (%)	Bar/T (%)	Bulge r_e (")	Bulge r_e (kpc)	Bulge n	Disk h (")	Disk h (kpc)	Bar r_e (")	Bar r_e (kpc)	Bar n
(1)	(2)	(3)	(4)	(5)	(6)	(7)	(8)	(9)	(10)	(11)	(12)	(13)
NGC3893	Bulge+Disk	34.40	65.60	0.00	15.95	1.04	3.68	20.52	1.34	-	-	-
NGC3938	Bulge+Disk	9.09	90.90	0.00	7.93	0.42	1.85	34.11	1.81	-	-	-
NGC3949	PSF+Bulge+Disk	7.75	92.20	0.00	4.67	0.22	0.64	15.22	0.72	-	-	-
NGC4027	Bar+Disk	0.00	79.50	20.50	-	-	-	43.11	2.03	26.50	1.25	1.80
NGC4030	Bulge+Disk	37.40	62.60	0.00	4.75	0.48	2.89	18.81	1.90	-	-	-
NGC4051	PSF+Bulge+Disk+Bar	13.50	52.50	34.00	9.21	0.44	0.93	55.66	2.64	68.08	3.23	0.45
NGC4062	Bulge+Disk	1.76	98.20	0.00	3.00	0.15	1.11	35.02	1.79	-	-	-
NGC4123	PSF+Bulge+Disk+Bar	6.87	79.20	13.90	6.55	0.56	0.59	56.76	4.84	42.98	3.66	0.46
NGC4145	PSF+Bulge+Disk	7.75	92.30	0.00	12.90	0.82	0.68	63.59	4.05	-	-	-
NGC4151	PSF+Bulge+Disk+Bar	41.30	50.30	8.42	9.36	0.62	0.44	37.74	2.49	57.00	3.76	0.10
NGC4212	Bulge+Disk	3.66	96.30	0.00	1.06	0.01	1.83	22.55	0.13	-	-	-
NGC4254	Bulge+Disk	39.30	60.70	0.00	31.30	5.17	2.81	33.83	5.58	-	-	-
NGC4293	PSF+Bulge+Disk+Bar	8.49	61.70	29.80	8.00	0.40	0.99	58.26	2.88	55.17	2.73	0.46
NGC4303	Bulge+Disk+Bar	8.28	82.80	8.91	2.67	0.30	1.55	44.58	4.93	32.35	3.58	0.55
NGC4314	Bulge+Disk+Bar	40.80	38.30	20.90	21.59	1.43	3.78	79.81	5.30	50.56	3.36	0.39
NGC4394	Bulge+Disk+Bar	18.10	68.10	13.80	4.84	0.26	3.41	44.87	2.39	29.52	1.57	0.62
NGC4414	PSF+Bulge+Disk+Bar	11.50	83.90	4.65	3.50	0.17	1.72	21.27	1.05	17.66	0.87	0.05
NGC4450	PSF+Bulge+Disk+Bar	16.90	71.50	11.60	8.19	1.10	2.26	47.16	6.33	36.13	4.85	0.33
NGC4487	Bulge+Disk+Bar	1.68	93.90	4.45	4.42	0.32	1.39	27.84	1.99	12.00	0.86	0.40
NGC4490	Bulge+Disk	6.76	93.20	0.00	21.14	0.87	0.40	44.01	1.80	-	-	-
NGC4527	Bulge+Disk+Bar	18.20	63.80	17.90	5.17	0.61	1.99	55.52	6.59	41.19	4.89	0.50
NGC4548	PSF+Bulge+Disk+Bar	13.00	68.60	18.40	6.97	0.23	1.56	58.22	1.96	44.91	1.51	0.51
NGC4593	PSF+Bulge+Disk+Bar	25.10	28.10	46.70	5.27	0.97	1.04	33.07	6.11	41.94	7.75	0.64
NGC4618	PSF+Bar+Disk	0.00	86.10	13.90	-	-	-	46.22	8.54	17.05	3.15	0.66
NGC4643	Bulge+Disk+Bar	25.00	54.10	20.90	5.43	0.52	2.53	48.22	4.64	21.30	2.05	0.62
NGC4647	Bulge+Disk	33.40	66.60	0.00	12.90	1.26	1.61	42.63	4.17	-	-	-
NGC4651	PSF+Bulge+Disk	41.70	58.30	0.00	18.52	1.01	0.63	30.46	1.66	-	-	-
NGC4654	Bulge+Disk	2.91	97.10	0.00	8.87	0.64	2.85	28.64	2.07	-	-	-
NGC4665	Bulge+Disk+Bar	15.20	67.00	17.80	6.57	0.36	2.10	53.31	2.89	29.37	1.59	0.79
NGC4689	Bulge+Disk	5.94	94.10	0.00	7.74	0.81	1.78	42.48	4.45	-	-	-
NGC4691	Bulge+Disk+Bar	17.90	69.20	12.90	12.24	0.93	0.84	33.70	2.57	25.29	1.93	0.43
NGC4698	Bulge+Disk	29.60	70.40	0.00	9.53	0.68	4.60	27.38	1.95	-	-	-
NGC4699	Bulge+Disk+Bar	19.90	76.50	3.59	2.62	0.27	2.08	15.93	1.62	13.49	1.37	0.02
NGC4772	PSF+Bulge+Disk+Bar	34.20	51.60	14.20	9.29	0.67	1.49	58.16	4.17	52.58	3.77	0.50

Table 2—Continued

Galaxy Name	Best Fit	B/T (%)	D/T (%)	Bar/T (%)	Bulge r_e (")	Bulge r_e (kpc)	Bulge n	Disk h (")	Disk h (kpc)	Bar r_e (")	Bar r_e (kpc)	Bar n
(1)	(2)	(3)	(4)	(5)	(6)	(7)	(8)	(9)	(10)	(11)	(12)	(13)
NGC4775	Bulge+Disk	31.20	68.80	0.00	21.55	2.33	1.91	18.30	1.97	-	-	-
NGC4781	Bulge+Disk	12.50	87.50	0.00	13.68	1.19	1.46	33.12	2.88	-	-	-
NGC4818	PSF+Bulge+Disk+Bar	7.04	73.70	19.20	2.82	0.21	0.47	36.31	2.69	16.38	1.21	0.51
NGC4856	Bulge+Disk+Bar	17.90	61.60	20.40	4.16	0.36	2.46	30.41	2.62	11.77	1.01	0.75
NGC4902	Bulge+Disk+Bar	6.24	83.80	9.98	3.60	0.67	2.58	30.52	5.69	14.11	2.63	0.37
NGC4930	Bulge+Disk+Bar	35.90	52.80	11.30	12.69	2.23	4.15	74.64	13.14	37.48	6.60	0.35
NGC4939	PSF+Bulge+Disk	21.40	78.60	0.00	9.52	2.01	2.78	32.14	6.79	-	-	-
NGC4941	PSF+Bulge+Disk	15.10	84.90	0.00	4.30	0.25	0.84	23.23	1.36	-	-	-
NGC4995	PSF+Bulge+Disk+Bar	6.62	87.20	6.20	4.14	0.50	0.05	19.56	2.34	18.03	2.16	0.34
NGC5054	Bulge+Disk	9.64	90.40	0.00	5.28	0.65	2.42	52.65	6.48	-	-	-
NGC5085	Bulge+Disk	6.04	94.00	0.00	5.53	0.74	1.48	33.88	4.55	-	-	-
NGC5101	Bulge+Disk+Bar	50.40	28.50	21.20	14.31	1.81	4.09	30.81	3.89	38.56	4.87	0.36
NGC5121	PSF+Bulge+Disk	36.40	63.60	0.00	4.68	0.48	2.41	15.62	1.61	-	-	-
NGC5161	Bulge+Disk+Bar	3.71	81.20	15.10	2.71	0.45	2.23	44.74	7.37	19.48	3.21	0.32
NGC5247	Bulge+Disk	7.88	92.10	0.00	9.69	0.91	1.59	59.30	5.57	-	-	-
NGC5371	Bulge+Disk+Bar	8.95	75.80	15.30	3.13	0.55	1.68	56.31	9.93	23.82	4.20	1.12
NGC5427	Bulge+Disk	15.40	84.60	0.00	9.55	0.90	3.14	27.27	2.56	-	-	-
NGC5483	Bulge+Disk+Bar	0.98	91.30	7.73	3.23	0.39	1.22	23.25	2.83	8.74	1.06	0.32
NGC5643	PSF+Bulge+Disk+Bar	8.21	81.80	10.00	5.68	0.46	2.14	45.30	3.63	48.58	3.89	0.43
NGC5676	Bulge+Disk	6.99	93.00	0.00	3.35	0.49	2.03	23.16	3.40	-	-	-
NGC5701	PSF+Bulge+Disk+Bar	24.40	63.50	12.10	11.13	1.19	2.41	70.67	7.56	26.01	2.78	0.40
NGC5713	Bulge+Disk	34.40	65.60	0.00	16.89	2.18	2.71	17.50	2.26	-	-	-
NGC5850	Bulge+Disk+Bar	16.30	64.20	19.60	6.76	1.15	2.64	77.55	13.19	47.27	8.04	0.91
NGC5921	PSF+Bulge+Disk+Bar	10.40	70.50	19.10	2.55	0.26	1.97	40.88	4.10	35.05	3.51	0.92
NGC5962	Bulge+Disk+Bar	10.30	78.80	10.90	2.33	0.32	1.37	14.56	1.99	13.85	1.89	0.02
NGC6215	Bulge+Disk	7.05	92.90	0.00	2.44	0.25	1.23	14.06	1.47	-	-	-
NGC6221	Bulge+Disk+Bar	5.27	82.00	12.80	3.16	0.29	2.73	51.47	4.78	19.33	1.80	0.87
NGC6300	Bulge+Disk+Bar	5.43	88.50	6.07	5.49	0.42	3.14	58.07	4.44	30.87	2.36	0.41
NGC6384	Bulge+Disk	27.90	72.10	0.00	15.66	1.82	3.13	40.05	4.65	-	-	-
NGC6753	Bulge+Disk+Bar	3.84	68.00	28.10	1.09	0.23	1.17	20.61	4.43	8.57	1.84	1.12
NGC6782	Bulge+Disk+Bar	35.50	49.50	15.00	5.06	1.34	2.39	28.20	7.48	21.48	5.70	0.37
NGC6902	PSF+Bulge+Disk	40.50	59.50	0.00	12.68	2.43	3.03	30.13	5.77	-	-	-
NGC6907	Bulge+Disk+Bar	10.90	63.20	25.90	3.45	0.74	1.53	29.20	6.24	23.66	5.05	0.34
NGC7083	Bulge+Disk	18.90	81.10	0.00	8.76	1.83	3.15	22.83	4.77	-	-	-

Table 2—Continued

Galaxy Name (1)	Best Fit (2)	B/T (%) (3)	D/T (%) (4)	Bar/T (%) (5)	Bulge r_e (") (6)	Bulge r_e (kpc) (7)	Bulge n (8)	Disk h (") (9)	Disk h (kpc) (10)	Bar r_e (") (11)	Bar r_e (kpc) (12)	Bar n (13)
NGC7205	Bulge+Disk	5.99	94.00	0.00	4.12	0.42	1.56	30.96	3.16	-	-	-
NGC7213	PSF+Bulge+Disk	65.70	34.30	0.00	19.55	2.42	2.68	63.19	7.83	-	-	-
NGC7217	PSF+Bulge+Disk	53.70	46.30	0.00	21.07	1.36	2.21	26.84	1.73	-	-	-
NGC7412	Bulge+Disk+Bar	4.21	68.50	27.30	2.64	0.31	1.71	23.61	2.78	35.21	4.15	1.21
NGC7479	PSF+Bulge+Disk+Bar	8.76	63.50	27.70	6.00	0.98	1.09	37.59	6.17	40.63	6.67	0.47
NGC7552	Bulge+Disk+Bar	23.40	61.10	15.50	2.70	0.31	0.64	17.54	1.99	42.05	4.78	0.24
NGC7723	Bulge+Disk+Bar	5.12	84.90	9.93	1.84	0.24	1.18	21.70	2.82	21.70	2.82	0.92
NGC7727	Bulge+Disk	75.00	25.00	0.00	20.27	2.56	4.85	24.29	3.06	-	-	-
NGC7741	Bulge+Disk+Bar	3.09	89.00	7.90	9.51	0.50	0.31	60.98	3.18	30.02	1.56	0.40
NGC7814	Bulge+Disk	37.60	62.40	0.00	9.39	0.67	2.10	31.17	2.24	-	-	-

Note. — Columns are : (1) Galaxy name. (2) The best fit chosen based on the criteria outlined in §3.3. (3) B/T, the fractional luminosity in the bulge. For objects with extra PSF component, the PSF luminosity is added to B/T. (4) D/T, the fractional luminosity in the disk. (5) Bar/T, the fractional luminosity in the bar. (6) Bulge effective radius in arcseconds. (7) Bulge effective radius in kpc, calculated from the angular diameter distance assuming a Hubble constant of 70 km s^{-1} Mpc^{-1}. (8) Bulge Sérsic index. (9) Disk scalelength in arcseconds. (10) Disk scalelength in kpc. (11) Bar effective radius in arcseconds. (12) Bar effective radius in kpc. (13) Bar Sérsic index.

Table 3. Checking GALFIT Robustness With Different Input Guesses

Galay (1)	Stage 3 Input/Output (2)	B/T (3)	Bulge r_e (") (4)	Bulge n (5)	D/T (6)	Disk h (") (7)	Bar/T (8)	Bar r_e (") (9)	Bar n (10)
NGC 4548	Input from 1D decomposition	17.5%	7.39	1.17	63.5%	28.4	19.0%	37.5	0.54
NGC 4548	Input from Stage 2	11.1%	7.50	1.70	69.9%	64.5	19.1%	37.5	0.54
NGC 4548	Stage 3 Output	13.0%	6.98	1.56	68.6%	58.2	18.4%	44.9	0.51
NGC 4643	Input from 1D decomposition	33.6%	7.18	0.86	40.4%	37.5	26.0%	22.0	0.60
NGC 4643	Input from Stage 2	24.1%	5.30	2.5	51.8%	46.4	24.1%	22.0	0.60
NGC 4643	Stage 3 Output	25.0%	5.43	2.53	54.1%	48.2	20.9%	21.3	0.62

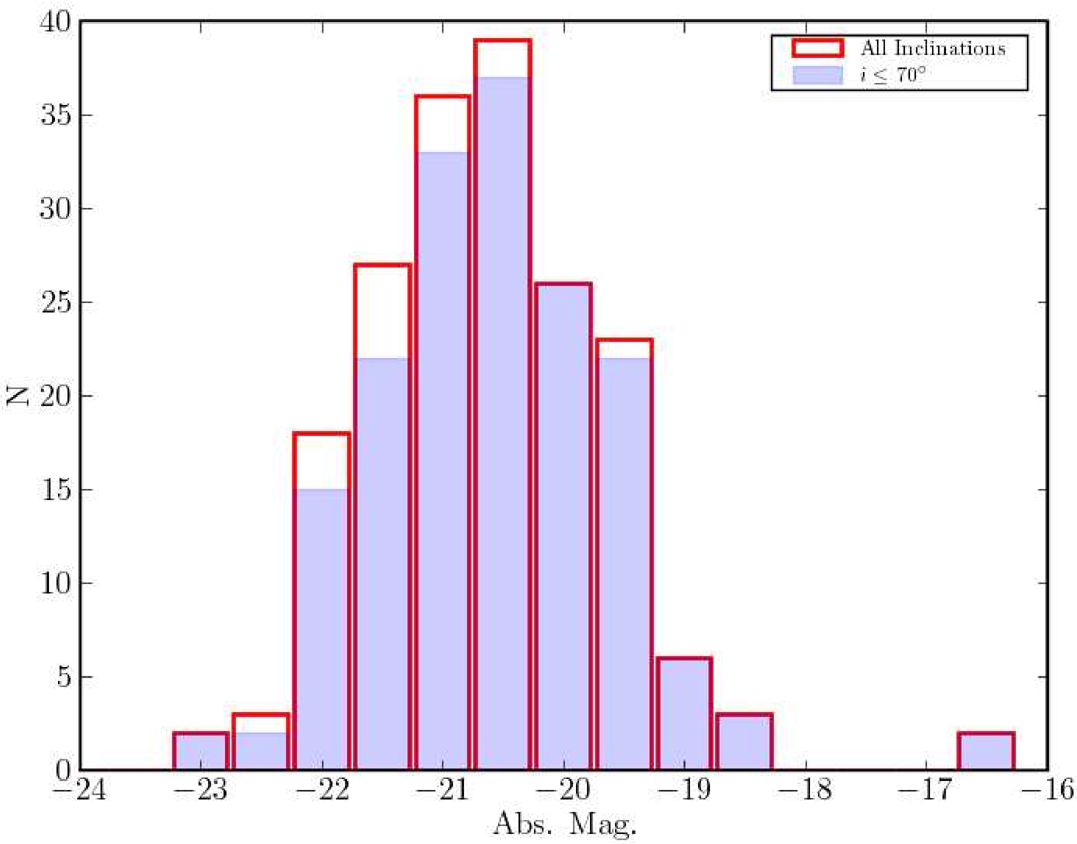

Fig. 1.— The distribution of absolute B-band magnitudes for the OSUBSGS sample before (unshaded) and after (shaded) the cut to remove highly inclined ($i > 70°$) spiral galaxies.

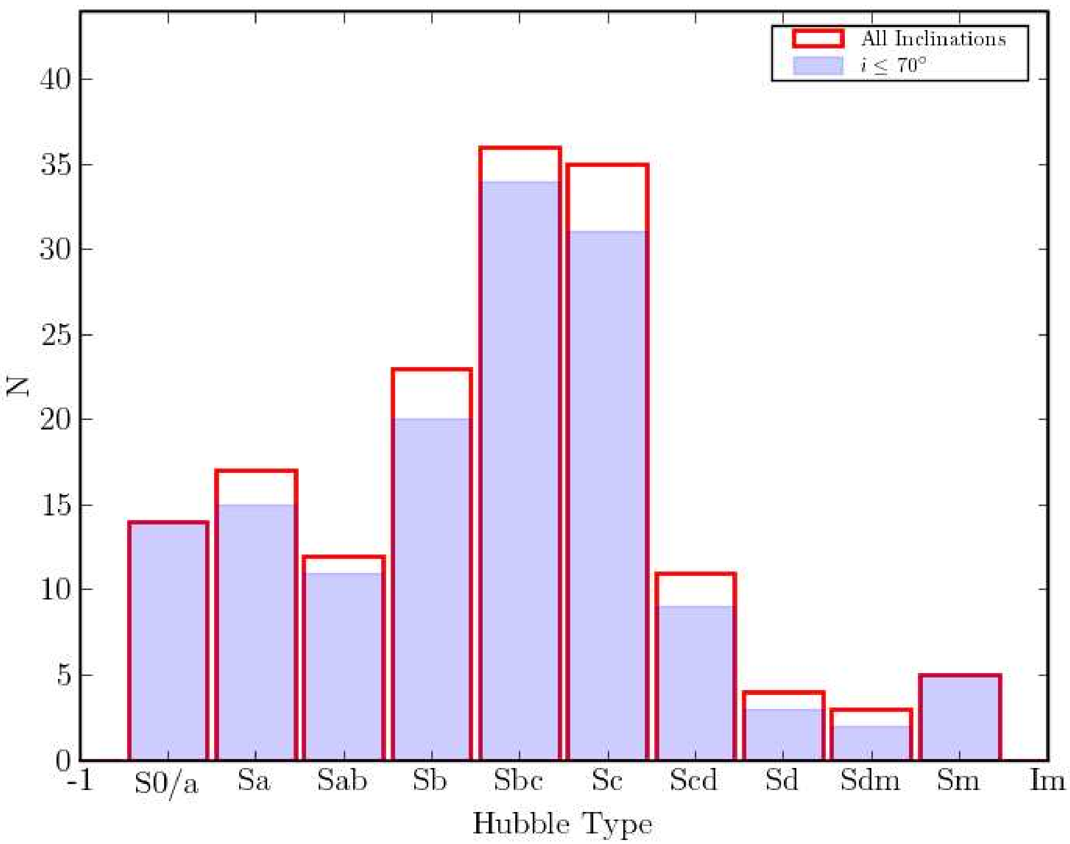

Fig. 2.— The distribution of Hubble types for for the OSUBSGS sample before (unshaded) and after (shaded) the cut to remove highly inclined ($i > 70°$) spiral galaxies. The sample is dominated by Hubble types S0/a to Sc.

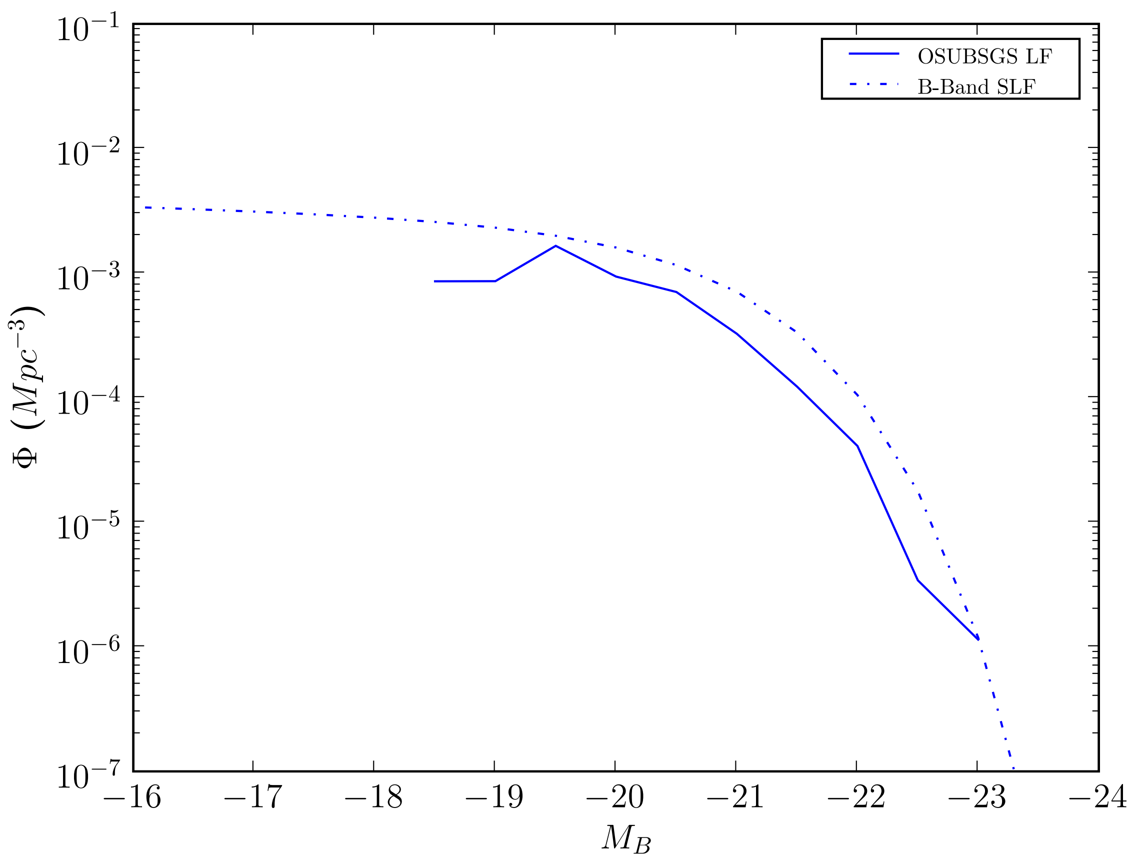

Fig. 3.— The OSUBSGS luminosity function is compared the B-band Schechter luminosity function (SLF). The former is calculated as described in §2.1 using equation (1). The parameters for the SLF are $\Phi^* = 5.488 \times 10^{-3}$ Mpc^{-3}, $\alpha = -1.07$, and $M_B^* = -20.5$, corresponding to H_0=70 km/s Mpc^{-1}.

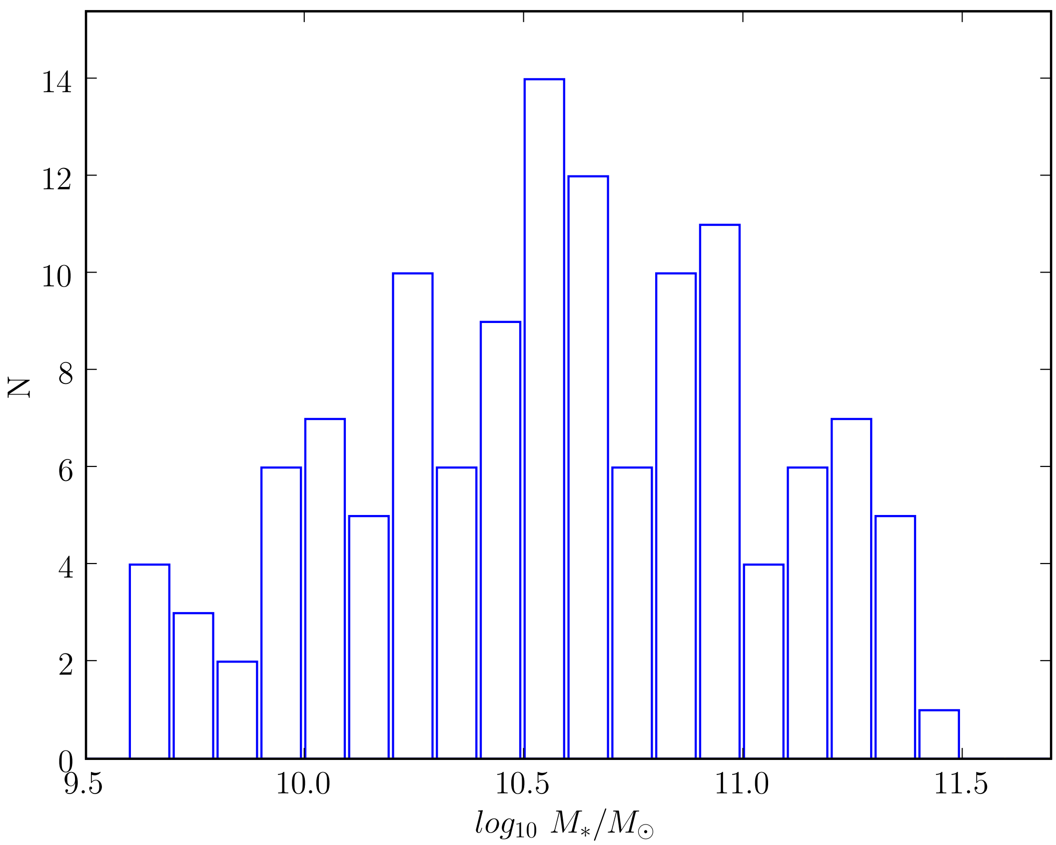

Fig. 4.— Stellar mass distribution of OSUBSGS galaxies as determined in §2.2.

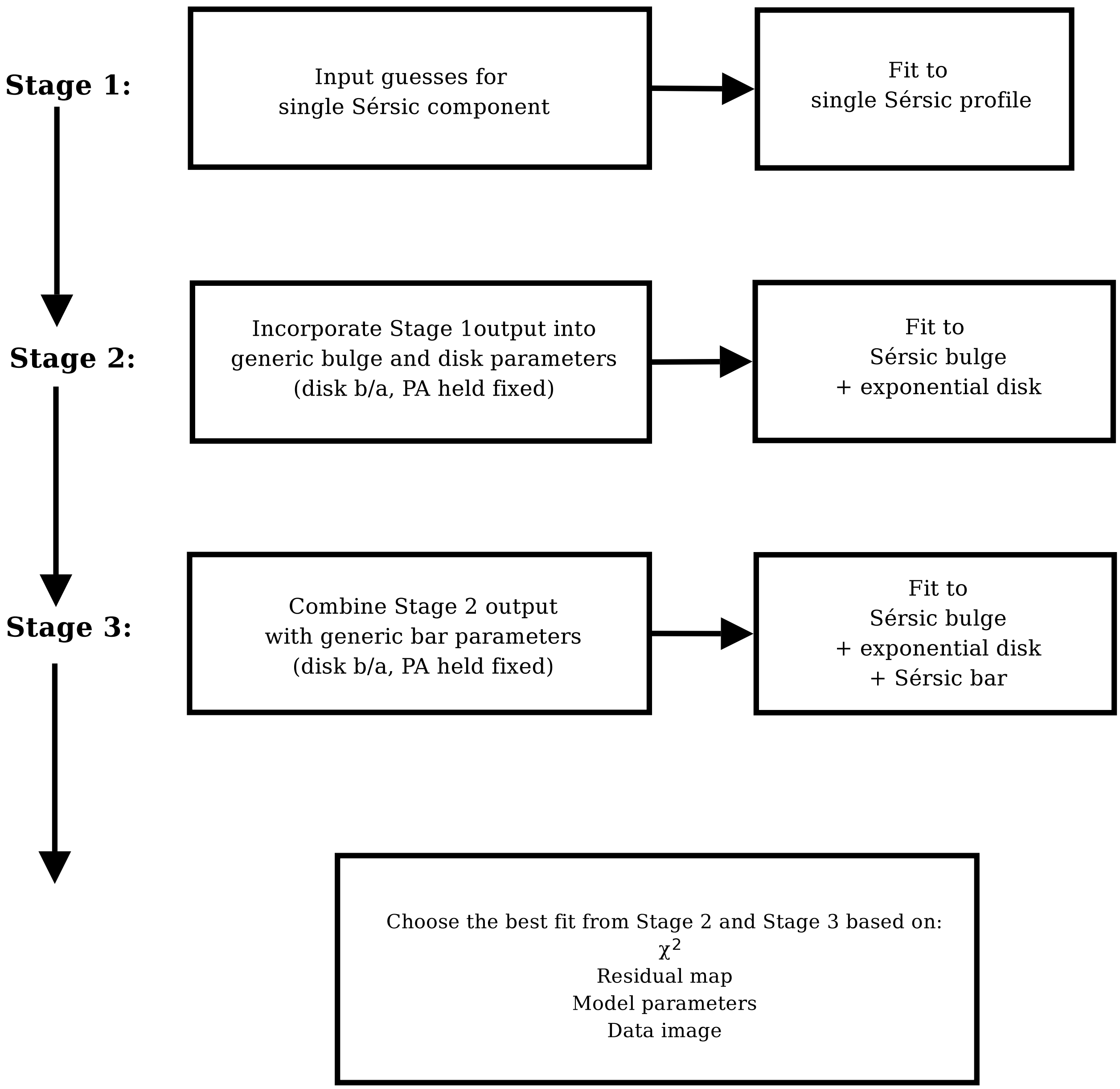

Fig. 5.— An overview of the method of decomposition. All images are subjected to Stages 1-3. Either the output of Stage 2 or Stage 3 is chosen as the best model.

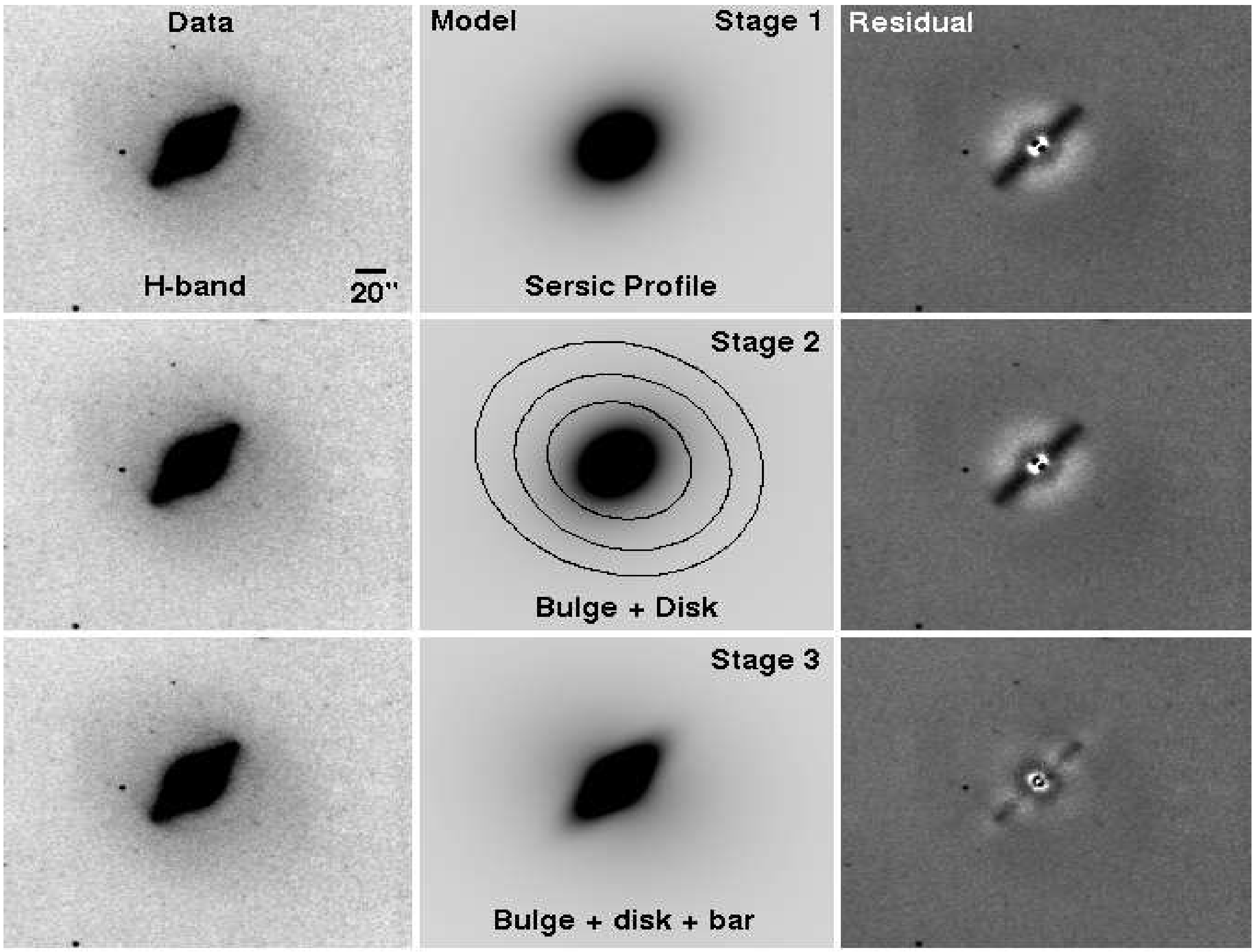

Fig. 6.— Complete 2D decomposition for NGC 4643. Note the prominent bar residuals in the residual for the Stage 1 and Stage 2 bulge-disk decomposition. This is a case where the prominent bar causes the Stage 2 bulge-disk fit to artificially extend the bulge and inflate the B/T. The disk fitted in Stage 2 has a low surface brightness and is very extended, well beyond the real disk: the b/a and PA of the fitted disk is shown as contours. Stage 3 bulge-disk-bar decomposition provides the best model. See Table 4 for the fit parameters.

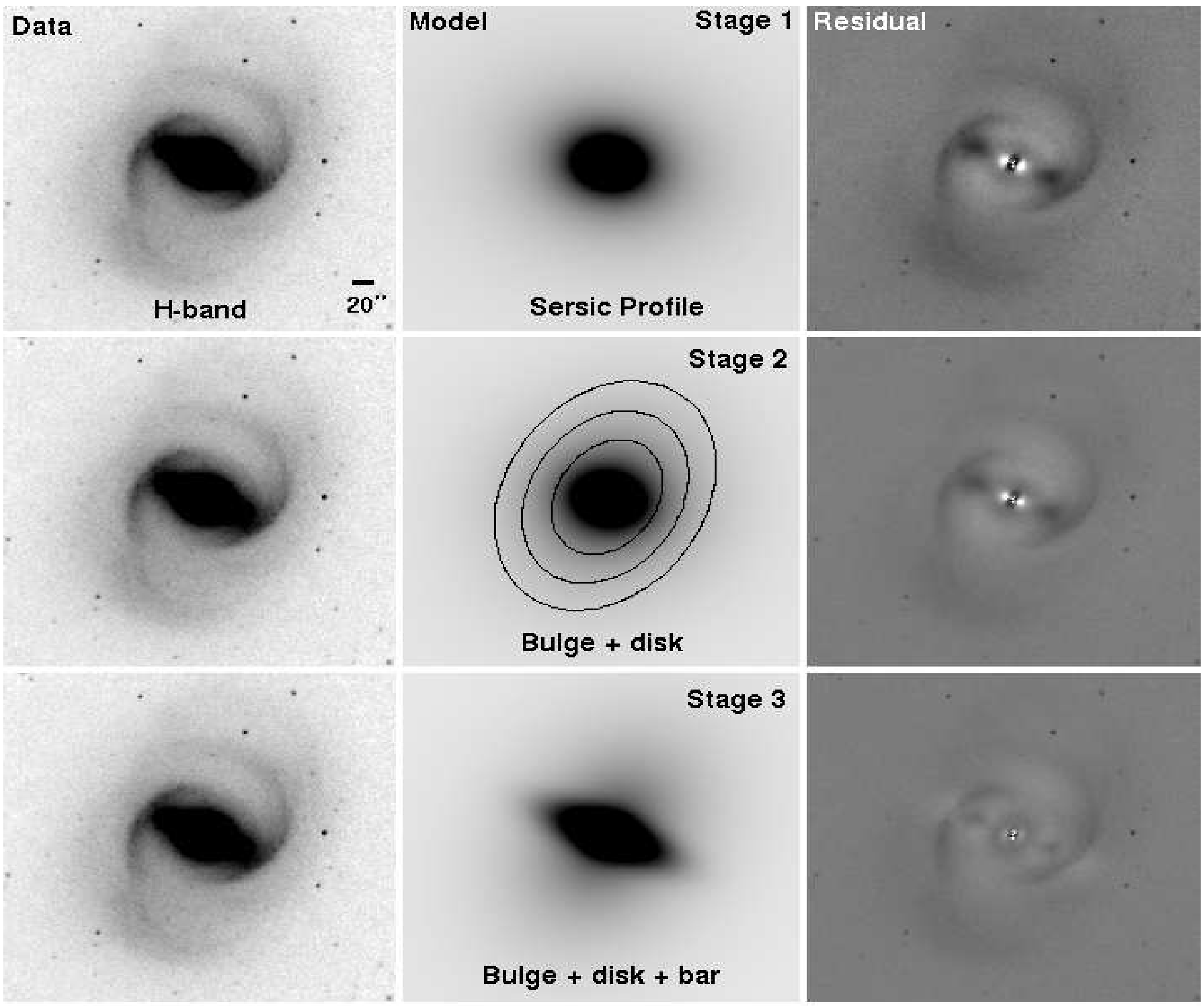

Fig. 7.— The complete $2D$ decomposition for NGC 4548. This is an extreme example where the prominent bar results in an extended bulge and inflated B/T in the Stage 2 bulge-disk fit. Like NGC 4643 in Figure 6, the disk fitted in Stage 2 has a low surface brightness and is very extended: its b/a and PA are shown as contours. Stage 3 bulge-disk-bar decomposition provides the best model. See Table 5 for the fit parameters.

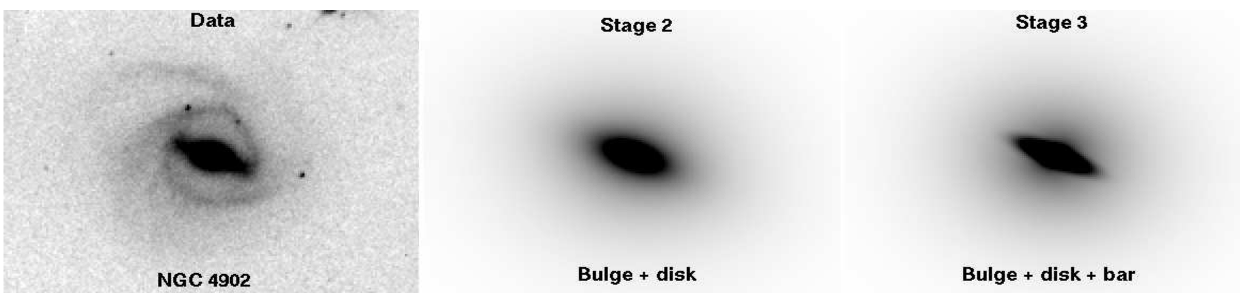

Fig. 8.— This plot shows the data image, Stage 2 model, and Stage 3 model for NGC 4902. The Stage 2 bulge is too bright and is extended along the major axis of the bar (B/T=31.2% and b/a=0.45). In Stage 3, the bulge and bar are fit with distinct components (B/T=6.2%, bulge b/a=0.75, Bar/T=10.0%, bar b/a=0.25).

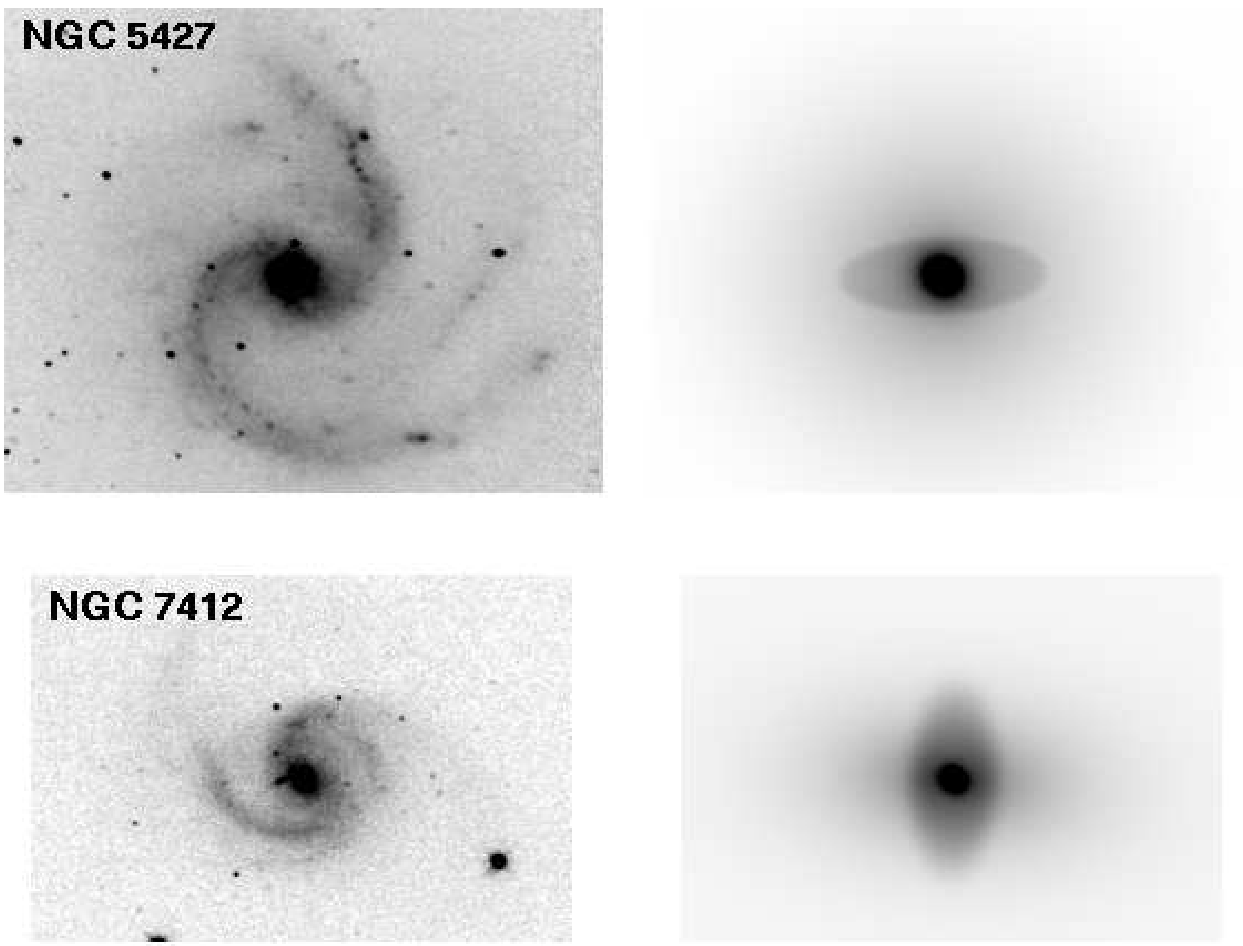

Fig. 9.— The data images and Stage 3 bulge-disk-bar decomposition models of NGC 5427 and NGC 7412 are shown. The Stage 3 models each distinctly show a false bar component, which is not present in the data images.The false components can be inspired by prominent spiral arms, such as those present in these galaxies. Such cases are flagged during the visual inspection of fits and the Stage 3 bulge-disk-bar decomposition is discarded in favor of the Stage 2 bulge-disk decomposition.

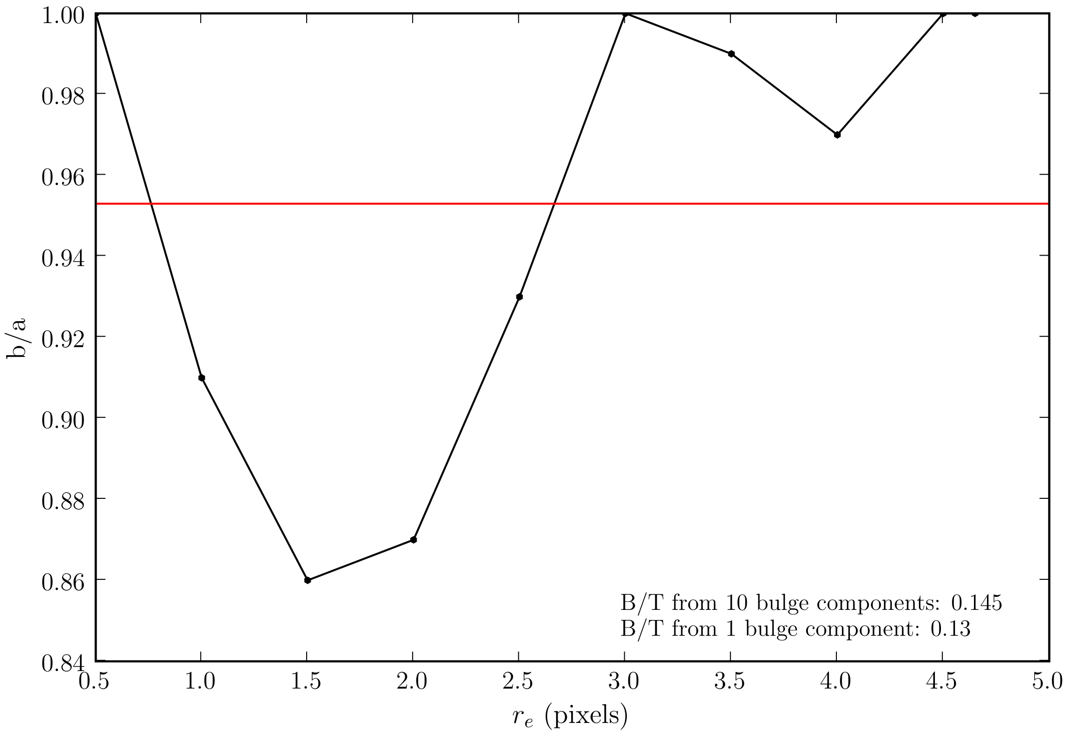

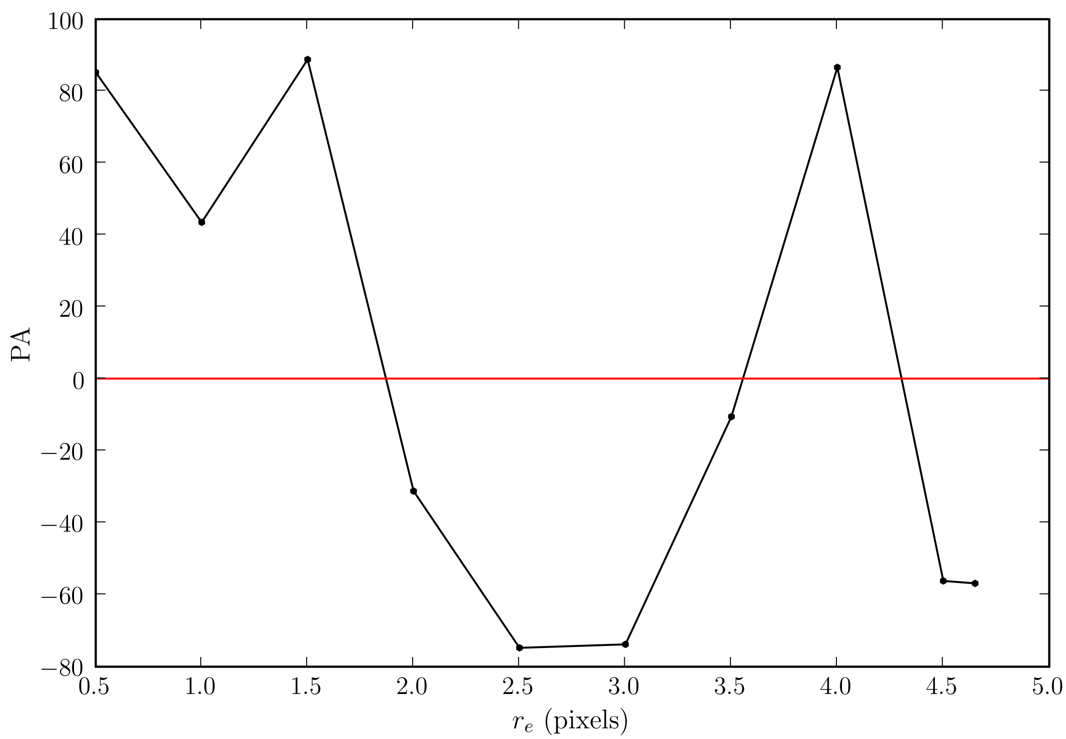

Fig. 10.— The run of b/a and PA are shown from modeling the bulge of NGC 4548 with ten concentric Sérsic profiles with fixed r_e each separated by 0.75". The mean b/a and PA are indicated with horizontal lines. The combined B/T from the ten components is 14.5%, in good agreement with the 13.0% value from the fit with a single bulge of constant b/a.

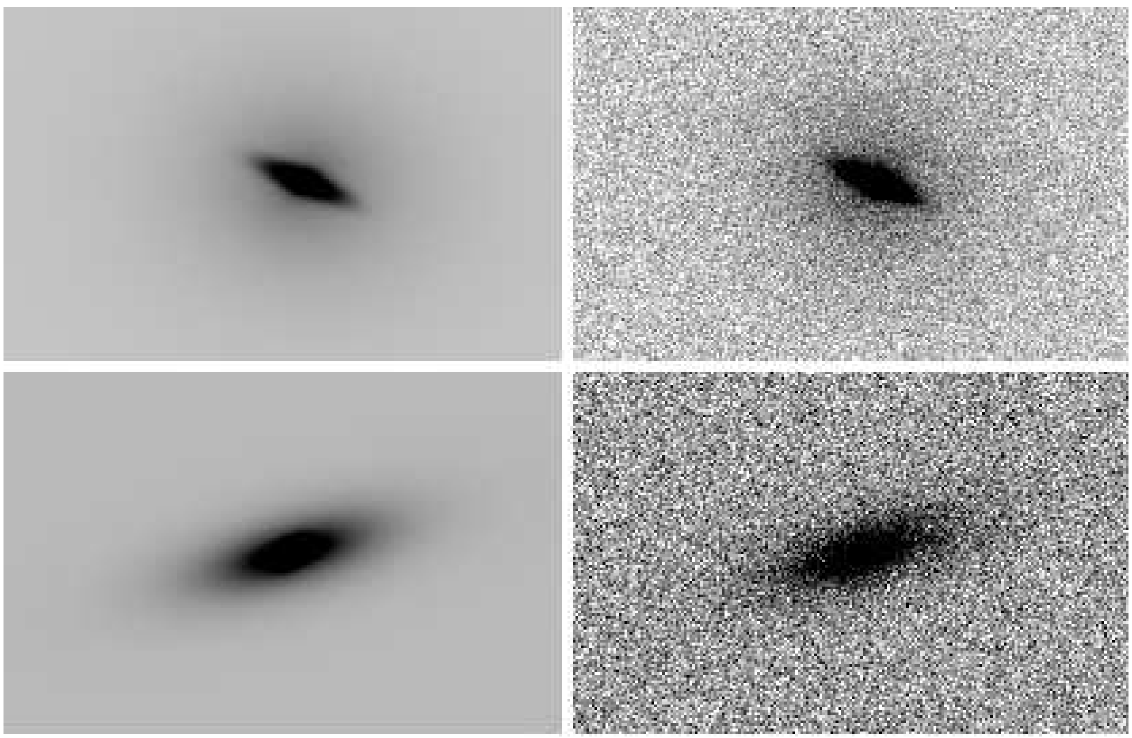

Fig. 11.— An elementary test is to determine if GALFIT can recover the known parameters of artificial noisy images. Noisy images were simulated by taking parametric model images (left panels) produced by GALFIT, and adding noise and sky background (right panels). The noisy images were then fitted to see if the original known parameters can be recovered. See §4.2 for details.

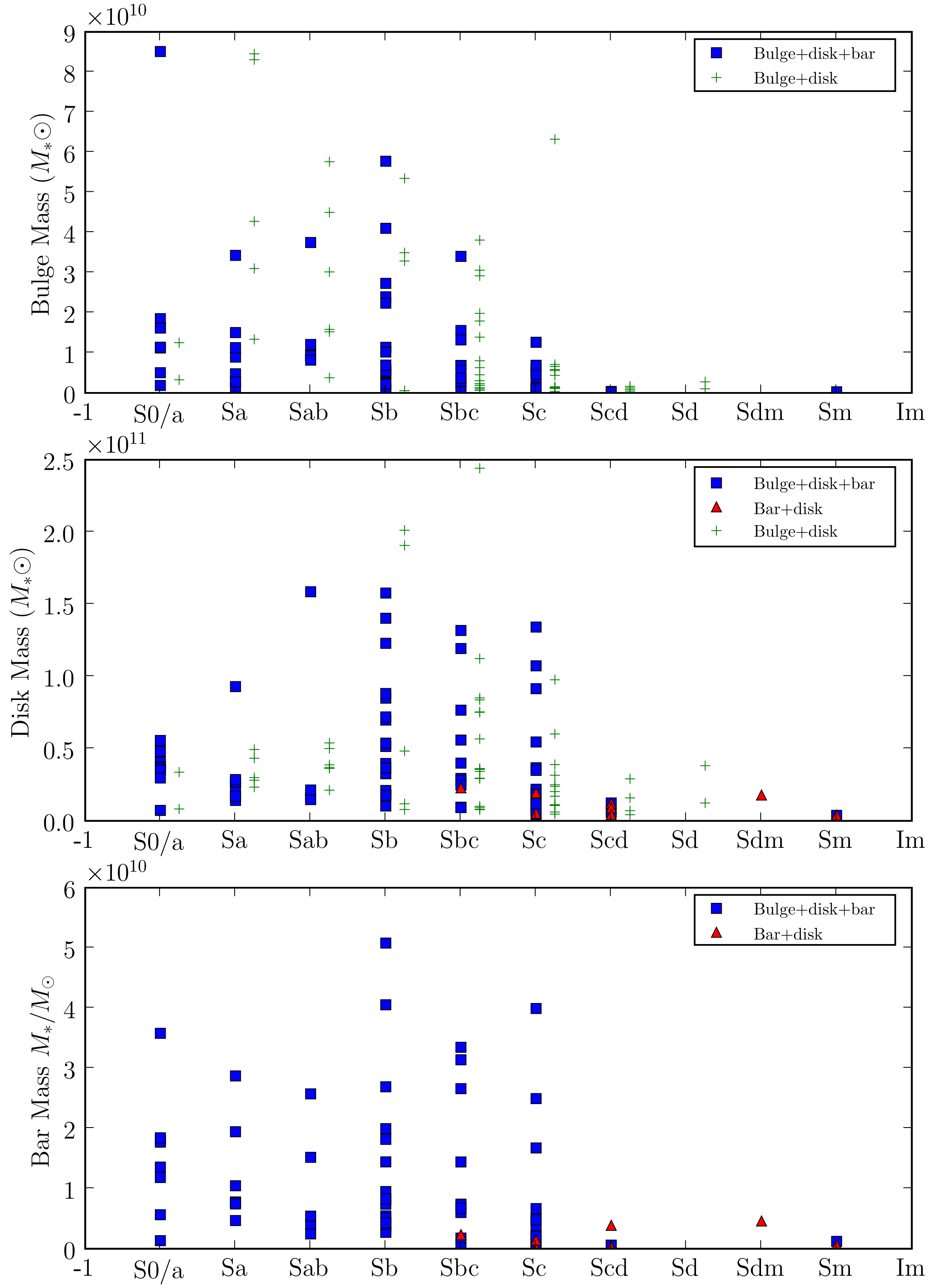

Fig. 12.— The top, middle, and bottom panels show stellar mass for bulges, disks, and bars, respectively, along the Hubble sequence.

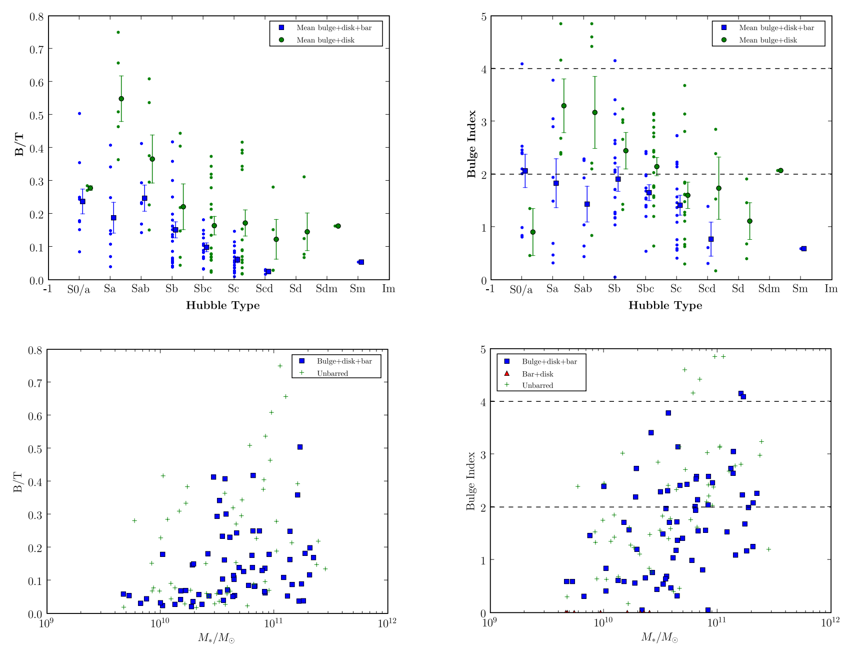

Fig. 13.— The individual and mean B/T (left panels) and bulge Sérsic index (right panels) are plotted, as a function of Hubble type and galaxy stellar mass. Barred and unbarred galaxies are shown separately. The mean B/T and bulge index in barred galaxies differ systematically from unbarred galaxies, but there is a large overlap in the individual values. The error bars denote the error on the mean. The distribution of B/T shows that bulges with

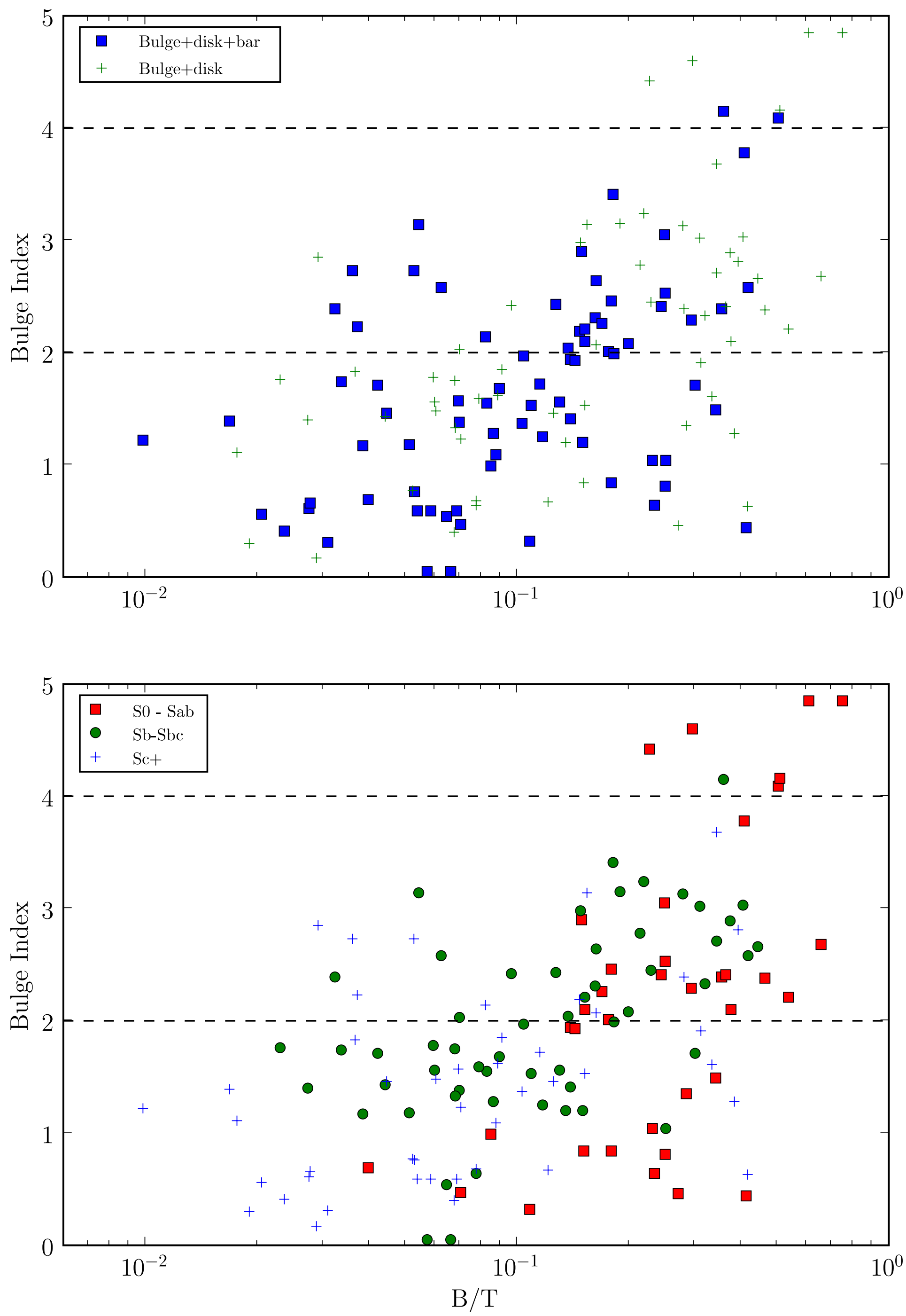

Fig. 14.— The relation between B/T and bulge index is shown. In the top panel, galaxies are coded according to bar class. In the lower panel, galaxies are coded according to Hubble type. Only a small fraction (5.5%) of bulges have classical Sérsic indexes ($n \geq 4$): such bulges lie primarily in S0/a to Sab,and have large $B/T > 0.2$. A large fraction (34.4%) of bulges have $2 < n < 4$: they exist in barred and unbarred S0/a to Sd, and their B/T spans a wide range with a mean of 0.23. Finally, 60.2% of bulges have $n \leq 2$: they exist in barred and unbarred galaxies across all Hubble types; their B/T spans a wide range (0.01 to 0.4) with a mean of 0.10.

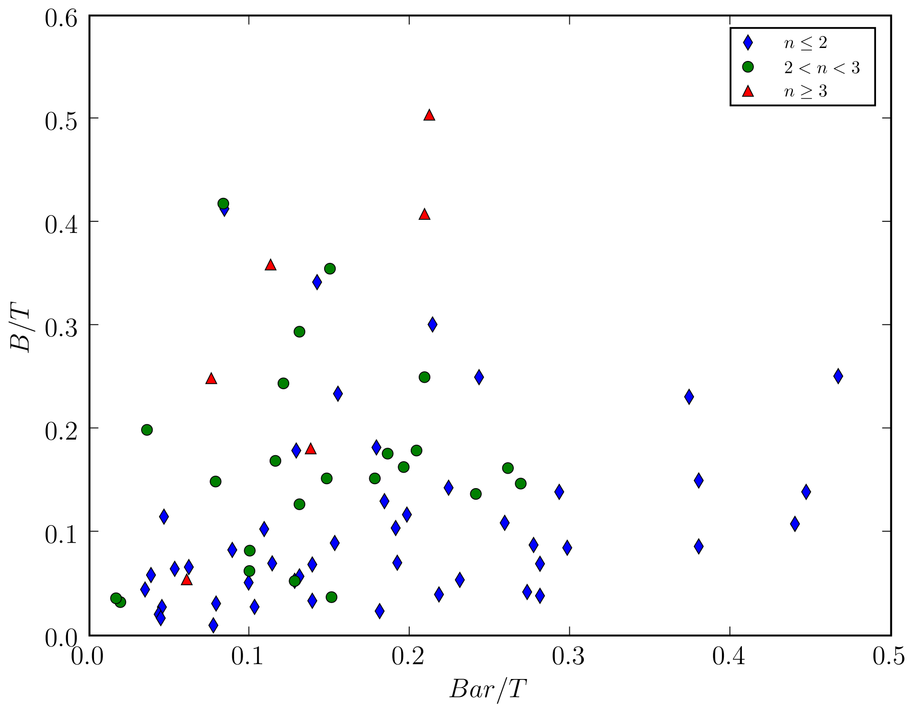

Fig. 15.— B/T is plotted against Bar/T and sorted by bulge Sérsic index. Aside from the eight galaxies with large Bar/T (≥ 0.3), most galaxies have moderate Bar/T and a wide range of B/T is seen at each Bar/T.

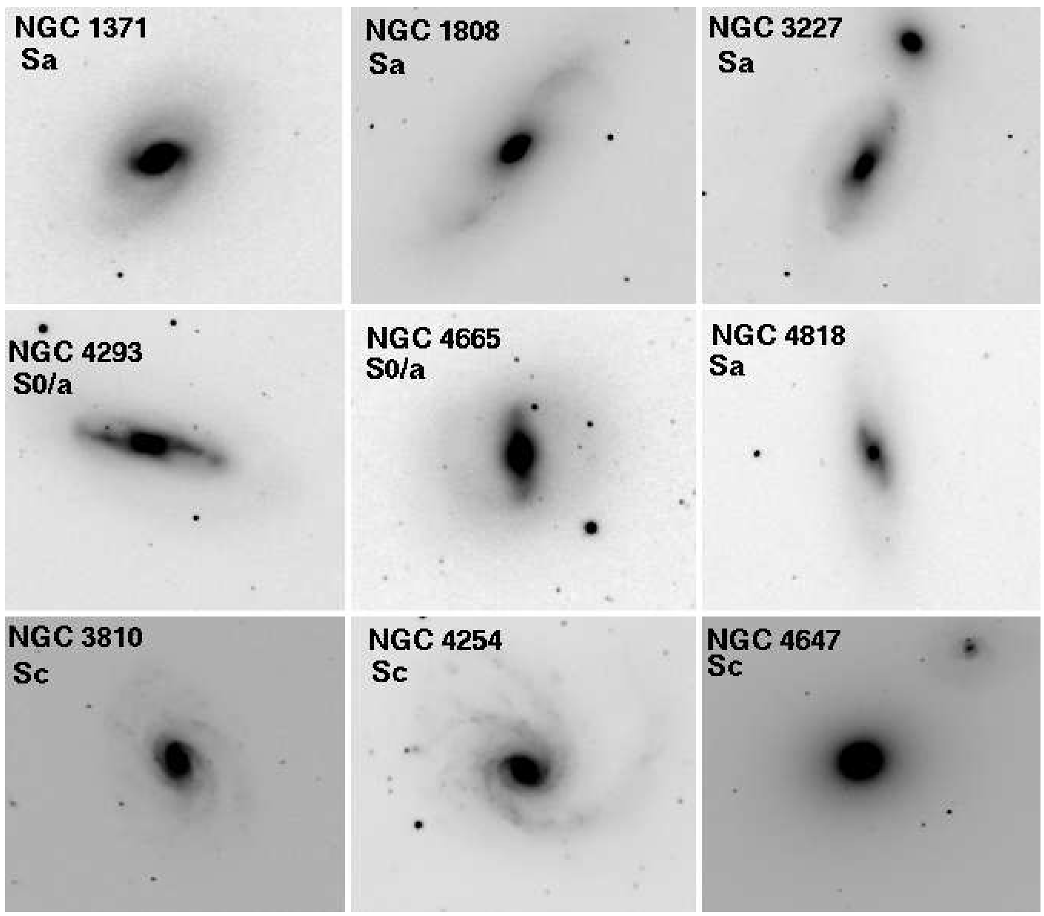

Fig. 16.— The top two rows contain barred galaxies, which have early RC3 Hubble types, but yet have $B/T < 0.2$. The bottom row contains unbarred galaxies, which have late RC3 Hubble types, but yet have $B/T \sim 0.4$. See § 5.3 for details.

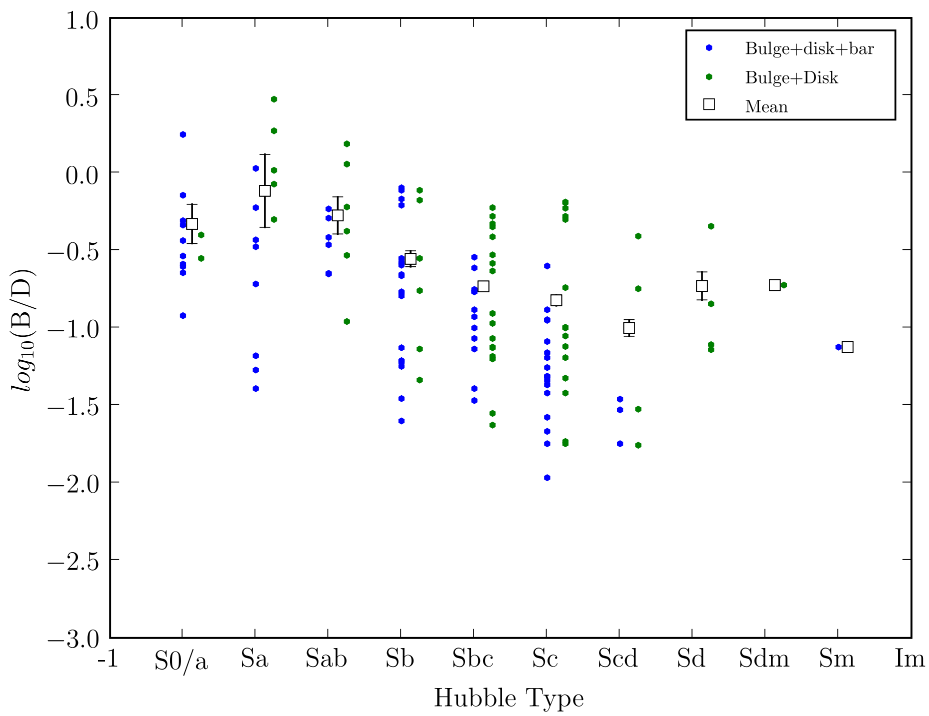

Fig. 17.— B/D is plotted against Hubble type for our sample. Barred and unbarred populations are separated, but the mean values for barred and unbarred together in each bin are shown.This plot can be compared against the corresponding plot in Graham (2001), based on a smaller sample of galaxies. Our mean H-band B/D ratios are comparable to the the means K-band B/D in Graham (2001). Both studies also find that B/D shows a large range for each Hubble type, while the mean B/D declines from Sa to Sc galaxies.

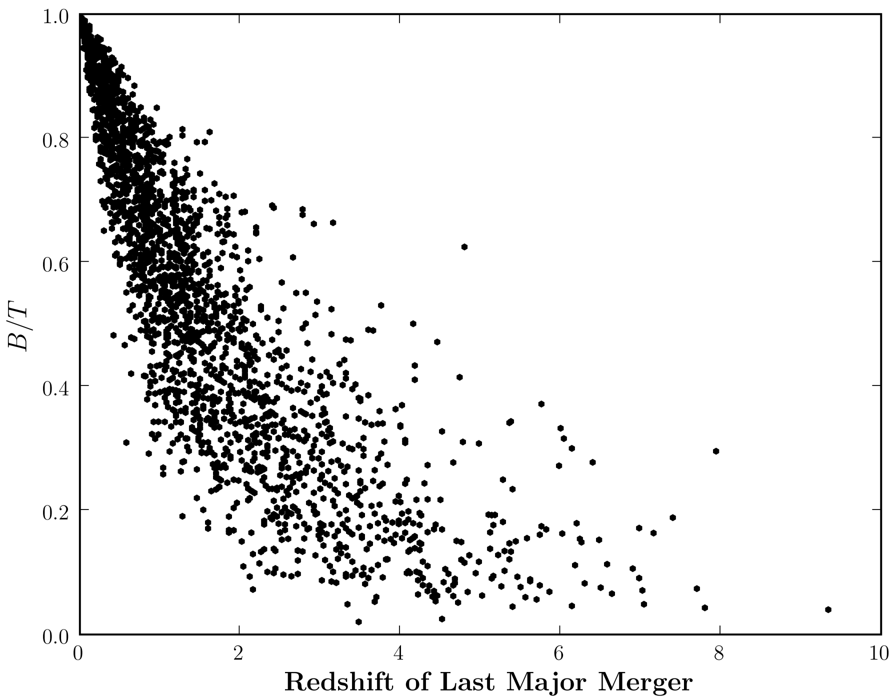

Fig. 18.— This figure shows B/T plotted against the redshift of the last major merger for the models described in §5.5 and shown in Figure 19. Galaxies with more recent major mergers are bound to have higher B/T because less time is available for disks to be built.

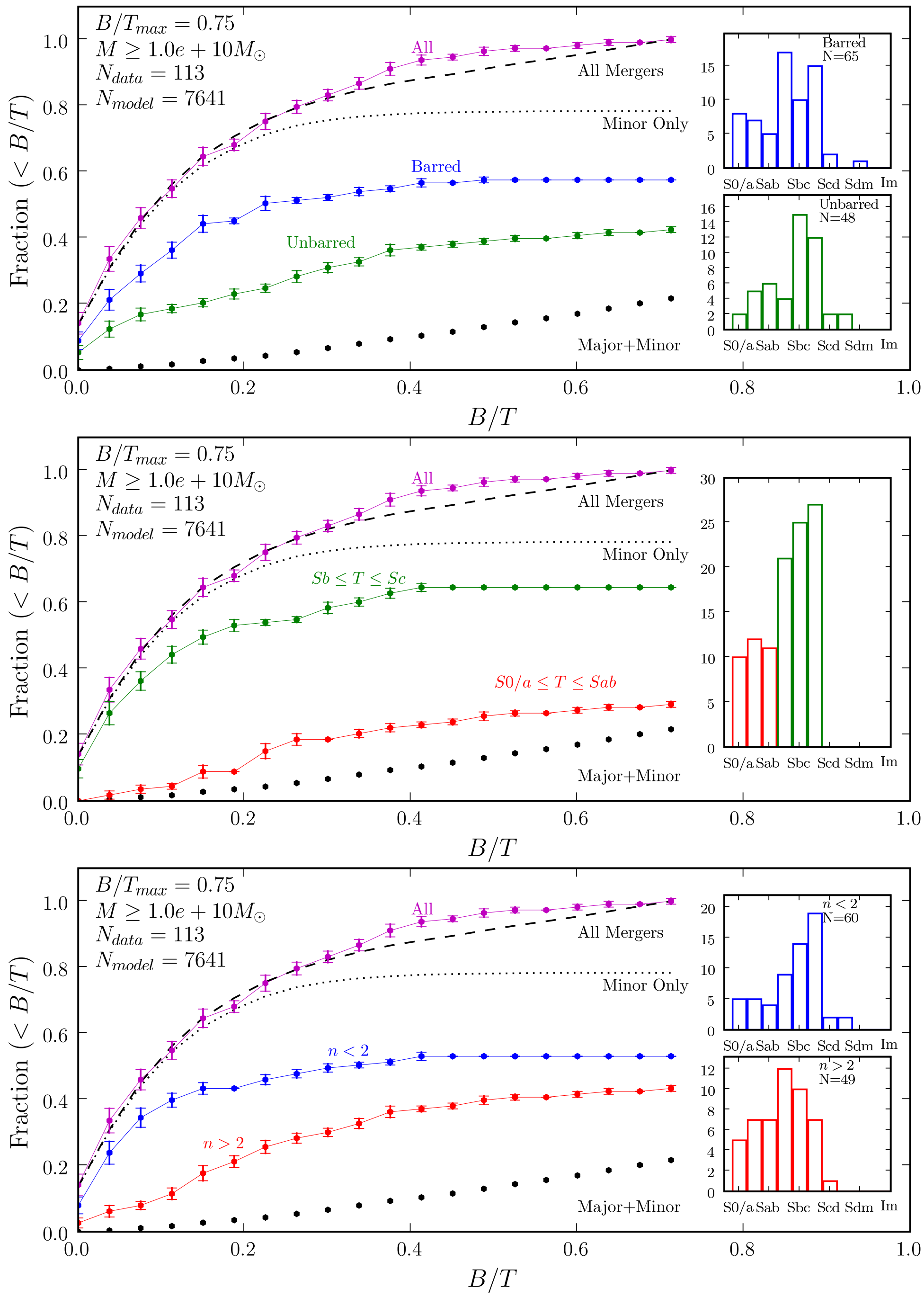

Fig. 19.— For galaxies with total stellar mass $M_* \geq 1.0 \times 10^{10} M_{\odot}$, this figure shows the observed cumulative fraction (solid line with symbols) of spiral galaxies with $B/T \leq 0.75$ (the limit on B/T is imposed to exclude any ellipticals produced in the models). The three panels are identical but sorted by bar class, Hubble type, and bulge Sérsic index. The dashed line is the cumulative fraction of B/T in spirals predicted by cosmological semi-analytical models from Burkert & Khochfar (2008, in prep.) for the same stellar mass range. The dotted line denotes those systems having only minor mergers, while the thick dots denote systems having both major and minor mergers. About 20% of spirals experience a major merger. These models assume every major merger of mass ratio $M_1/M_2 \geq 1/4$ produces a spheroid with $B/T \sim 1$.

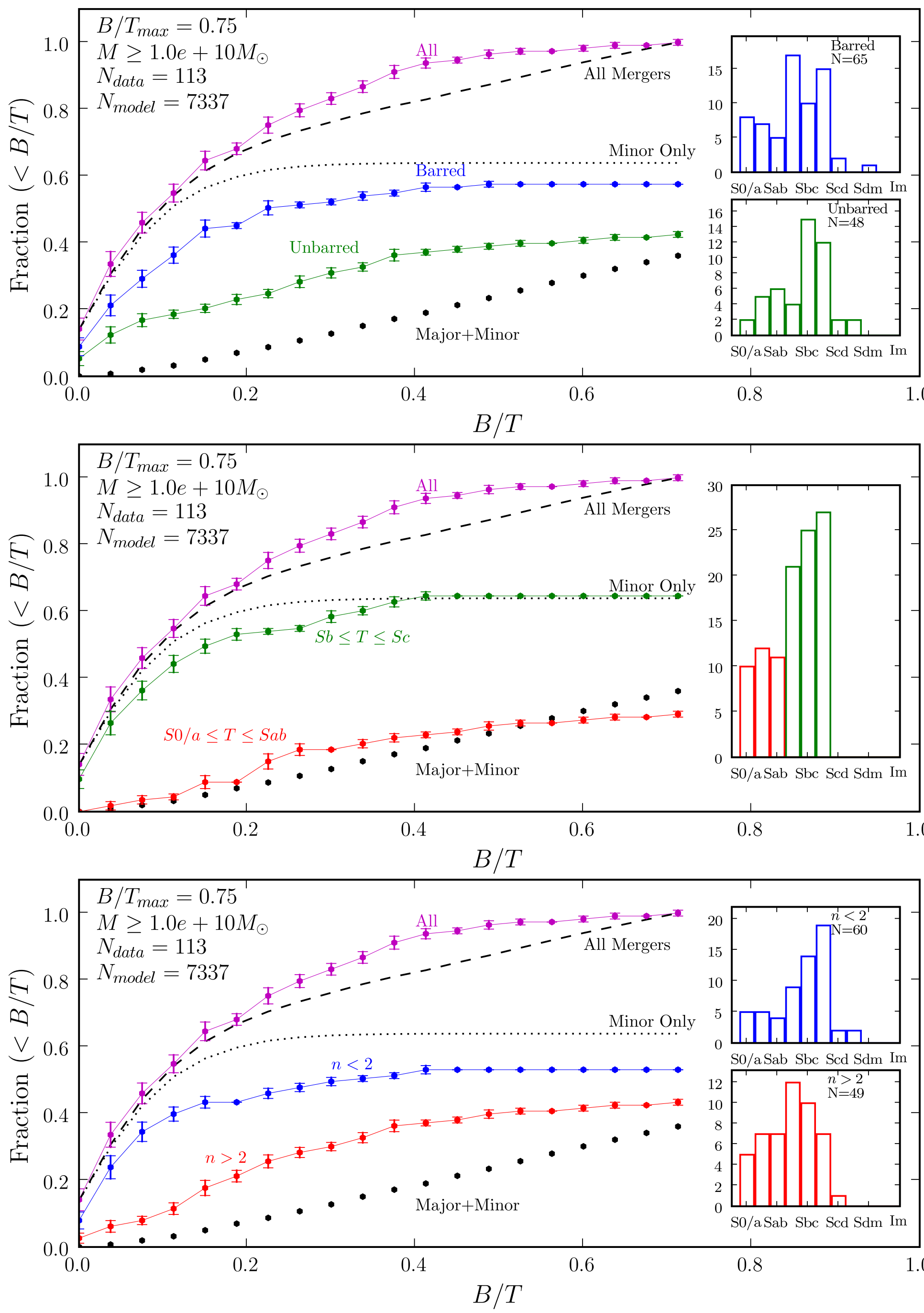

Fig. 20.— This panel is calculated identically to Figure 19, except that the condition for disk destruction in major mergers has been relaxed to mass ratio $M_1/M_2 \geq 1/6$. In this case, about 30% of spirals undergo major mergers. The model underpredicts the data by about 10% near $B/T = 0.4$. Since the "Minor Only" curve lies so near the $Sb \leq T \leq Sc$ and $n < 2$ curves, such systems are likely built from a combination of major and minor mergers, but predominantly by mergers with $M_1/M_2 < 1/6$.

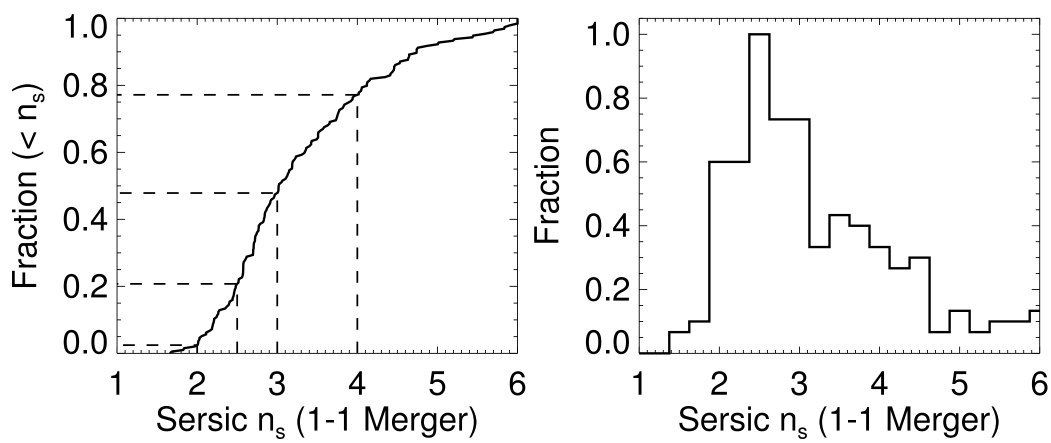

Fig. 21.— We show the distribution of Sérsic indexes derived by fitting a single Sérsic index to a representative set of 1:1 merger remnants in the simulations of Hopkins et al. 2008 (in prep). Note that while $\sim$ 22% of the remnants have classical $n > 4$, as much as 20% have low $n < 2.5$, while 50% have $n < 3$. This suggests that intermediate $2 < n < 4$ bulges can result from major mergers that have residual gas left-over after violent relaxation. [Figure: courtesy of Phil Hopkins]

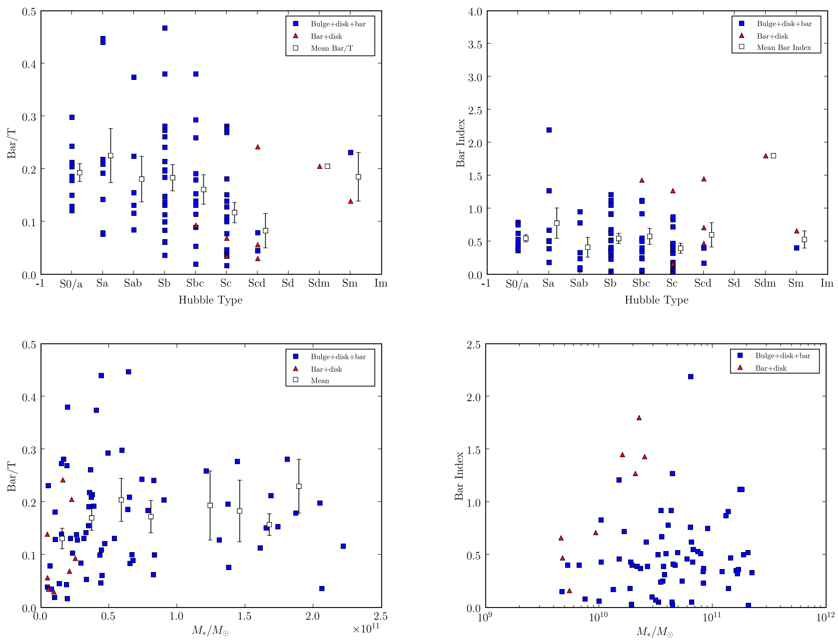

Fig. 22.— Upper left: Mean and individual Bar/T plotted against Hubble type. Upper right: Mean and individual bar sérsic indexes plotted against Hubble type. Lower left: Bar/T plotted against total galaxy stellar mass. The mean Bar/T in bins of stellar mass is indicated. Lower right: Bar Sérsic index plotted against total galaxy stellar mass. All plots: The error bars where shown indicate error on the mean.

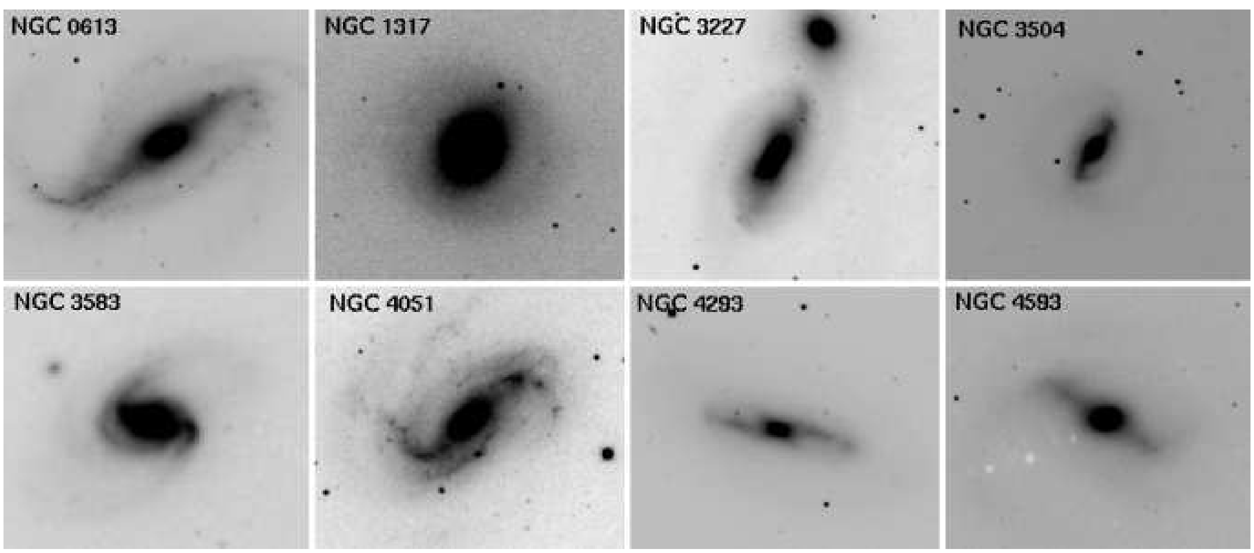

Fig. 23.— Systems with Bar/T near or above ~ 0.3.

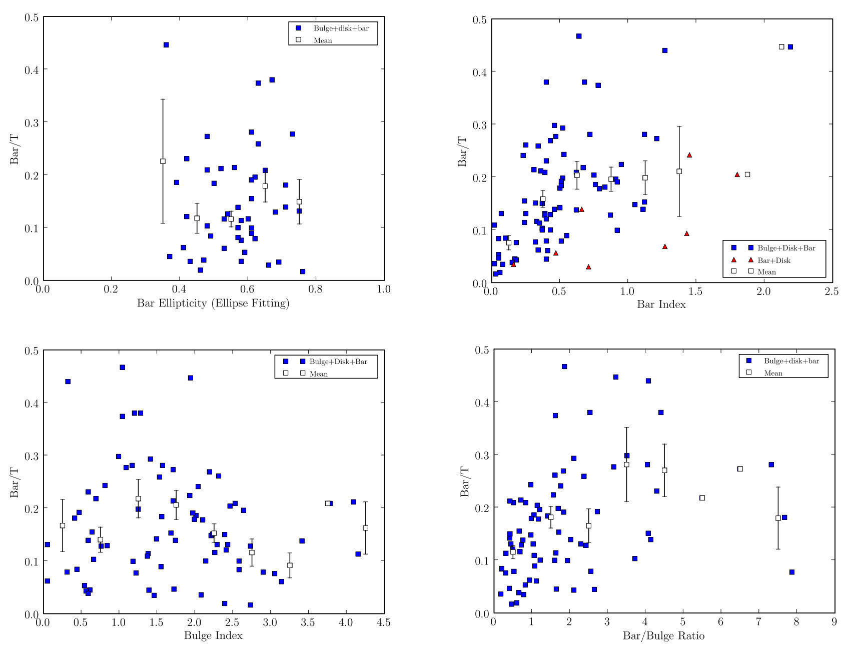

Fig. 24.— Upper left: Bar/T is plotted against peak bar ellipticity from MJ07. Upper right: Bar/T is plotted against bar Sérsic index. Lower left: Bar/T is plotted against bulge Sérsic index. Lower right: Bar/T is plotted against mean bar/bulge luminosity ratio. All plots: Mean Bar/T is calculated for bins along the ordinate axis. The error bars indicate error on the mean.

Table 4: Decomposition For NGC 4643

Fit		r_e or h ($''$)	r_e or h (kpc)	n	b/a	Position Angle	Fractional light
Stage 1	Sérsic	27.90	2.66	4.44	0.80	-51.03	100%
Stage 2	Bulge	23.86	2.30	4.16	0.80	-51.08	34.6%
	Disk	335.88	32.33	1.00	0.84	66.94	65.4%
Stage 3	Bulge	5.43	0.52	2.53	0.90	60.52	25.0%
	Disk	48.22	4.64	1.00	0.84	66.94	54.1%
	Bar	21.30	2.05	0.62	0.37	-45.84	20.9%

Table 5: Decomposition For NGC 4548

Fit		r_e or h ($''$)	r_e or h (kpc)	n	b/a	Position Angle	Fractional light
Stage 1	Sérsic	154.59	5.19	5.19	0.80	78.31	100%
Stage 2	Bulge	57.86	1.94	4.32	0.76	75.77	61.5%
	Disk	60.39	2.03	1.00	0.75	-32.54	38.5%
Stage 3	Bulge	6.98	0.23	1.56	0.88	-66.50	13.0%
	Disk	58.22	1.96	1.00	0.75	-32.54	68.6%
	Bar	44.91	1.51	0.51	0.35	66.65	18.4%

Table 6: Mass Breakdown of Galactic Structures for $M_* \geq 1.0 \times 10^{10} M_\odot$

Structure	Mass (%)
Bulges	20.4
Disks	69.6
Bars	10.0
Bulges with $n > 2$	15.7
Bulges with $n < 2$	4.7

Table 7: B/T : Data versus Hierarchical Models of Galaxy Evolution

B/T	Data (%)	Model (Major+Minor)(%)	Model (Minor Only)(%)
$B/T < 0.2$	66.4 ± 4.44	3.09	64.1
$0.2 \leq B/T < 0.4$	23.0 ± 3.95	5.80	13.1
$0.4 \leq B/T < 0.6$	7.96 ± 2.54	6.76	1.15
$0.6 \leq B/T < 0.75$	2.65 ± 1.51	6.02	0.03

Table 8: Bar Fraction as a Function of B/T and Bulge Index

Bulge n	Bar Fraction
$n \leq 2$	61% (48 of 79)
$2 < n < 4$	52% (27 of 52)
$n \geq 4$	29% (2 of 7)
B/T	Bar Fraction
$B/T < 0.2$	66% (61 of 93)
$0.2 \leq B/T < 0.4$	38% (12 of 32)
$B/T \geq 0.4$	31% (4 of 13)